The Potential for Terrestrial Storage of Woody Biomass from High Wildfire Risk Forests in the Western United States under Historical and Projected Future Climates

Leah K. Clayton

Advisor: Sinéad Crotty

Second Reader: Matthew Eisaman

A senior thesis presented to the faculty of the Department of Earth and Planetary Sciences, Yale University, in partial fulfillment of a Bachelor's Degree of Science.

Abstract

In this thesis, I present a geospatial modeling approach to understand the climatological potential for the terrestrial storage of woody biomass via burial under evapotranspiration (ET) covers in the Western US. Given the 21st century wildfire crisis, forest managers are implementing mechanical thinning to remove low-value woody biomass at unprecedented scales. Terrestrial storage of biomass (TSB) in the form of biomass burial represents a potential opportunity to durably store this photosynthetically-captured carbon. Soil water balance is critical to understand the potential for successful biomass burial. In the first section of this thesis, I develop an applied water model to temporally account for when snowfall reaches the water column and then use this applied water product with actual evapotranspiration (AET) to geospatially quantify water balance for 2001-2020 on a 1 km by 1 km scale. From this water balance, we calculate how much water would need to be stored in a monolithic soil cover to prevent the percolation of water assuming a potentially infinite water storage reservoir and then convert this required water storage to soil cover thickness. This analysis indicates that there are regions in the Western US that have soil water balance conditions conducive to woody biomass burial from a macroclimate perspective. In the second section of this thesis, I utilize the latest CMIP6 climate modeling under two emissions scenarios, SSP2-4.5 an SSP5-8.5, to understand how the potential for biomass burial is projected to change throughout the 21st century geospatially with a 0.25º by 0.25º resolution. We parameterize and build a geospatial implementation of the Penman (1948) potential evapotranspiration (PET) equation to project future evaporative demand. We use the ratio between projected precipitation and PET known as aridity index to geospatially identify regions where woody biomass burial appears feasible under future climate conditions.

Table of Contents

1. Introduction

In the Western United States, climate change is already causing warmer temperatures and an intensification of the hydrological cycle, resulting in severe drought, extreme precipitation events, earlier snowmelt, and increased atmospheric evapotranspirative demand (Martin et al., 2020; Milly and Dunne, 2020; Overpeck and Udall 2020; Allan and Douville 2023; Simpson et al., 2023). These changes are predicted to further intensify over time if greenhouse gas emissions are not abated.

Prolonged drought, climate change, and decades of fire suppression have resulted in overstocked forests and larger, more severe, and more destructive wildfires across the Western US since the turn of the century (USFS, 2022). Further climate change will likely only worsen this problem unless significant forest treatments are implemented (Abatzoglou and Williams, 2016). After two particularly intense fire years in 2020 and 2021, the US Forest Service released a report in 2022 titled “Confronting the Wildfire Crisis” wherein they detail an ambitious plan to remove over one billion bone-dry tonnes of woody biomass from high wildfire risk forests in the Western US within a decade of publication. Given the current dry, overstocked conditions of most forests in the Western US, prescribed burning is not a safe option to treat the land area necessary to meet the goals set out by the forest service. Instead, a dramatic increase in mechanical thinning will comprise most of the forest treatments. With mechanical thinning, the removed biomass is often low value and relatively small. As such, it is generally left to decay on-site or burned, which releases the carbon contained in the biomass back into the atmosphere as carbon dioxide or methane over varying time scales (Fingerman et al., 2023).

Given the large amount of low value biomass being removed from Western US forests and the need for carbon dioxide removal and storage to mitigate climate change, researchers have begun exploring pathways to durably store the photosynthetically captured carbon in woody biomass. In 2021, a team at Lawrence Livermore National Laboratory published a proposal for a carbon storage pathway called Biomass Carbon Removal and Storage (BiCRS) that describes the potential to utilize biomass, including thinned wood, to store carbon either belowground or in other long-term products (Sandalow et al. 2021). A recent paradigm called the Aines Principle suggests that at a high enough cost of carbon, it is economically favorable to use biomass for carbon storage as opposed to bioenergy (Woodall and McCormick, 2022). With the pressing need to reduce greenhouse gases in the atmosphere, biomass may now be more valuable for more carbon storage than for energy.

BiCRS presents several different options for durable storage of biomass including gasification, pyrolysis, and torrefaction, and recent research has indicated that these products can potentially serve as carbon sinks when properly implemented (Smith, 2016; Fingerman et al., 2023; Simões et al., 2023). While the products from these processes, such as biochar or biofuels, are either more stable or economically valuable, they require significant technology and infrastructure. Given the short time scale and large magnitude of the USFS plan, the variable spatial distribution of biomass to be removed across the Western US, and the lack of current infrastructure to support these technologically- and resource-intensive biomass conversion options, there is a need for a low-technology use case with a quick implementation timeline.

Terrestrial storage of biomass (TSB) via biomass burial has the potential to fill this near-term need. Carbon storage via biomass burial was first published in scientific literature by Zeng (2008), and it has been iterated on since by Zeng and others (Zeng et al., 2013; Zeng and Hausmann, 2022; Gooding, 2023). The basic implementation of burial of woody biomass involves the excavation of a chamber or vault that biomass is then placed in and covered with soil and potentially other engineered materials. The goal of burial is to create an anaerobic environment such that biomass decay does not occur, and thus, the carbon remains held in the biomass.

The cover above the biomass is a critical buffer to prevent the entrance of oxygen or moisture from the atmosphere into the burial vault to maintain a low moisture, anaerobic state. Extensive ecological literature indicates the controlling role of climate on decay pathways and rates dominant driver of decay rates (Meentemeyer, 1978; Gholz et al., 2000; Parton et al., 2007; Cusack et al., 2009; Joly et al., 2023).Dry conditions below a relative humidity threshold of 0.60 can essentially stop decay (Stevenson et al., 2015). Risks of decay include carbon dioxide and methane atmospheric emissions as well as carbon loss in leachate. Decay, especially along anaerobic pathways that produce methane, can result in a burial implementation being a carbon source instead of a carbon sink.

There are significant scientific gaps with respect to site selection and monitoring, reporting, and verifying (MRV) biomass burial implementations. Local climate plays a critical role in determining the conditions that a burial vault needs to be designed for, and ultimately, it should likely inform what sites are even considered for burial. It is critical to understand the amount and timing of any water reaching a cover, and this can be understood by assessing the soil water balance.

There are two main pathways currently used to quantify soil water balance. One pathway relies on highly simplified estimations using widely available soil and monthly meteorological data and empirical coefficients. This pathway is easy to implement, but the results are broad approximations of the water balance instead of useful quantifications, and it is generally used solely for a preliminary understanding of site conditions (Albright et al., 2010). The second pathway utilizes Richards' equation-based fluid flow models. These models, such as HYDRUS and UNSAT-H, are the gold standard to understand subsurface fluid flow with atmospheric forcing and specific soil conditions, but they require detailed parameterization of the soil and atmospheric forcing beyond what is available in geospatial databases or extensive assumptions (Fayer, 2000; Simunek et al., 2005). The requisite inputs for these models make it infeasible to apply them beyond the site level where detailed field and laboratory measurements can be made.

This thesis is primarily focuses on developing the necessary water balance and climatological models and methodologies relevant to creating a geospatial decision tool for siting woody biomass burial in the Western US. While there are many economic, ecologic, social, and physical factors that need to be accounted for before implementing woody biomass burial, climatological and water balance conditions can restrict whether burial for durable carbon storage is even plausible. I address both the recent water balance conditions derived from observational datasets as well as projected changes in conditions from future climate modeling.

In section 2, I develop a daily snow accumulation and melt model to quantify when water reaches the soil column and how this varies from the temporal distribution of precipitation. I then use this product, termed applied water, in a simplified daily water balance model with a daily actual evapotranspiration (AET) product and infinite storage water reservoir to calculate the required water storage and minimum required burial depth of a given area in a historical time period from 2001 to 2020. In order to understand the potential for durable carbon storage under changing climate conditions, in section 3, I quantify the potential change in suitability for biomass burial in the Western US using daily historical and projected climate data from 26 global circulation models (GCMs) under two greenhouse gas emissions scenarios from the most recent coupled model intercomparison experiment, CMIP6, by the IPCC. In this section, I first develop a geospatial implementation of a physically-based, potential evapotranspiration (PET) model using the Penman (1948) PET equation. I then analyze PET over time in relationship with precipitation in a ratio called aridity index to understand how future water balance may change from historical conditions.

2. Geospatial Implementation of Water Balance with Historical Data and the Implications for Woody Biomass Burial

2.1 Introduction

Within the framework of biomass carbon removal and storage (BiCRS), woody biomass burial emerges as a potentially viable near-term option for storing carbon from wood thinnings due to its potential to implemented on short-time scales, relative low-cost, and low reliance on specialized infrastructure. To prevent decay of the buried biomass, scientists and engineers have introduced the idea of using engineered covers that serve to protect the stored biomass from changes in moisture or oxygenation that would result in decay of the biomass carbon to methane or CO2. Various cover designs have been proposed, modeling the precedent of landfill design (Madalinski et al., 2003; Hauser et al., 2005). Broadly, these covers can be categorized into monolithic and layered covers. While layered covers contain horizons of different substrates, often including plastic textile barriers or rock of different clast size, monolithic covers solely rely on the soil column thickness and vegetation to protect the waste from decay (Gross, 2005).

Given that woody biomass burial for thinned wood is positioned as a low-cost, near-term storage method, the simplicity of monolithic covers is more suitable for woody biomass burial than highly engineered covers. Monolithic covers consider the water storage capacity of soil along with the evapotranspirative demand of the climate and vegetation to protect the buried material (Albright et al., 2010). These monolithic covers are also termed evapotranspiration (ET) covers (Madalinski et al., 2003; Hauser et al., 2005). The goal of an ET cover is to have a sufficient layer of soil that can store the required amount of water applied to a given area under the climatic conditions of that area to minimize water percolation to the stored waste. Ideally in the context of burial for durable carbon storage, monolithic covers would be designed with a soil cover thickness such that any water applied to the soil surface will not reach the biomass given the local climatologic, pedologic, and hydrologic conditions.

Across the Western US, there are different precipitation regimes that correspond to various climate phenomena and geophysical forcing. We define the Western US as the contiguous US states west of Colorado's eastern border: Montana, Wyoming, Colorado, New Mexico, Arizona, Utah, Idaho, Washington, Oregon, Nevada, and California. California has a summer dry season and winter wet season where most of the annual precipitation is received in winter, often in extreme precipitation events caused by atmospheric rivers (Dettinger, 2011; Kim et al., 2012; Huang et al., 2020). The coastal Pacific Northwest, including northern California, western Oregon, and western Washington receives high precipitation year-round, especially in the Coast and Cascade mountain ranges where the topography drives higher precipitation (Smith 2006). These regions are also affected by extreme precipitation events from atmospheric rivers (Leung and Qian, 2009; Neiman et al., 2011).

Prevailing westerly winds drive most of the precipitation in the intermountain region east of the Sierra Nevada and Cascade mountain ranges and west of the Rocky Mountains, as well as within the Rocky Mountains. Due to stronger midlatitude storms in the winter and spring, much of the precipitation in this zone occurs during those seasons (Lauenroth et al., 2014). It is highly orographically driven, and high points of elevation receive more precipitation and typically have rain shadows on the leeward side (Smith, 2006; Colle et al., 2012). The Great Plains east of the Rocky Mountains predominantly receive summer precipitation due to the summer weakening of the prevailing westerly winds, allowing the Atlantic subtropical high to spin warm, wet air off the Gulf of Mexico into the central US (Lauenroth and Bradford, 2006; Lauenroth et al., 2014). Many regions in the interior Western US receive very little precipitation (< 200 mm annually), including the Sonoran and Chihuahuan deserts. In the desert Southwest, the North American summer monsoon contributes most of the precipitation in summer storms (Adams and Comrie, 1997; Higgins et al., 1997). A vast majority of precipitation events in the Western US are small (<10 mm) (Lauenroth and Bradford, 2009).

In the Western US, snow plays a large role in the hydrological cycle and regional energy balance (Trujillo and Molotch, 2014). Snowpack affects the local energy balance by increasing the albedo, thereby reducing the amount of energy a region stores from solar radiation, and acting as an insulator such that ground temperatures beneath snow remain warmer than air temperatures (Milly and Dunne, 2020). In the context of ET covers, understanding snow is critically important because it serves to store water from when it was precipitated to a later date when it melts and reaches the soil column. The importance of snow is recognized in landfill literature, but it’s treatment in modeling is varies from the inclusion of simulated snowpack and snowmelt (Khire et al., 1997) to empirical parameterization based on a binary of whether or not a region receives snow at any point in the year (Albright et al., 2010).

The term applied water is used in waste containment literature to describe any water that reaches the waste cover (Bendz et al., 1998). The objective of this section of this thesis is to first develop a reasonable geospatial model for applied water that accounts for snowmelt using publicly available, meteorological data across the Western US. I then use the applied water product with evapotranspiration products to quantify pixel-by-pixel water balance over time. Several iterations of this modeling process are presented, and the final version incorporates a solar radiation-driven snowmelt model for applied water and a geospatial product for actual evapotranspiration. The second objective is to use the results of the water balance modeling to calculate the minimum ET cover thickness required to prevent the percolation of water to stored biomass geospatially across the Western US. Three versions of the final required cover thickness are presented: versions 1 and 2 represent early versions of a more primitive model while version 3 represents the most robust calculations.

2.2 Methods

2.2.1 Basis of Evapotranspiration Covers

The basis of the water balance for ET covers is described by Albright et al. (2010) in *Water Balance Covers for Waste Containment: Principles and Practice*. The authors derive the equations necessary to determine the approximate monthly required water storage, and thus required soil cover thickness, based on soil properties and historic meteorological data. The total water storage capacity (S_c) of a given soil is the depth-integrated volumetric soil water content at field capacity (θ_c), or the amount of water a layer of soil can hold up to the point of percolation to a greater depth (Equation 1). Field capacity water content is measured at 33 kPa suction by convention. Depth-integrated total water storage capacity is approximately equal to the field capacity water content of a given layer of soil times the depth (L) of that layer (Equation 1).

$$S_c = \int \theta_c dz \cong \theta_c L \tag{1}$$

However, not all of the storage capacity in the soil should be considered for an evapotranspiration cover because plants cannot access all water stored within the soil pores. The available storage capacity (S_a) is defined as the depth-integrated total storage capacity minus the water content that cannot be accessed by plants. This is described by equation 2,

$$S_a = \int(\theta_c - \theta_m)dz \;\cong\; (\theta_c - \theta_m)L \tag{2}$$

where θ_m is the volumetric soil water content at minimum storage, or the water content that cannot be removed by plants. Minimum storage water content is described by the wilting point, which is conventionally measured at 1500 kPa suction. At suction pressures higher than the wilting point, the water content of the soil is low enough that capillary action, and thus root water uptake, becomes impossible. The wilting point for plants in arid and semiarid climates can be at pressures as high as 8000 kPa due to plant adaptation to the dry conditions.

Given the goal of an ET cover to prevent the percolation of water through the soil to the biomass, the available storage capacity needs to be greater than or equal to the required water storage (S_r), as determined by the local climate. Equation 2 can be rearranged and combined with this constraint to provide a required depth of an ET cover where the available storage capacity is greater than or equal to the required storage (Equation 3).

$$L \geq \frac{S_r}{(\theta_c - \theta_m)} \tag{3}$$

Albright et al. determine required storage, S_r, using local climatological conditions on an annual time scale. They calculate monthly soil water storage (ΔS) requirements using a simple mass balance (Equation 4),

$$\Delta S = P - R - AET - L - P_r \tag{4}$$

where P is precipitation, R is runoff, AET is actual evapotranspiration, L is internal lateral drainage, and P_r is percolation. All quantities are cumulative for the given month and in units of depth (mm). However, given that most of these quantities are either very small or difficult to measure without extensive instrumentation on a site, Albright et al. present empirical equations with coefficients derived from Apiwantragoon (2007). The empirical equation is described by equation 5,

$$\Delta S = P - \beta PET - \Lambda \tag{5}$$

where P is monthly cumulative precipitation in mm, β is a dimensionless coefficient used to approximate AET from PET, PET is total monthly potential evapotranspiration in mm, and Λ is a loss term coefficient with units of depth (mm) that acts as a conservative estimate of both runoff and percolation. These coefficients β and Λ are calculated for two seasonal groupings for areas that have snow and frozen ground and those that don't (Table 1).

	Seasons	β (-)	Λ (mm)
No snow or frozen ground	Fall-Winter	0.30	27.1
	Spring-Summer	1.00	167.8
Snow or frozen ground	Fall-Winter	0.37	-8.9
	Spring-Summer	1.00	167.8

Table 1: Coefficients for approximating monthly soil water storage requirements using the empirically based equation 5. These approximations allow for calculation of monthly soil water storage with data that can be easily measured or calculated (precipitation and potential evapotranspiration). Fall-Winter Is defined as September through February (inclusive). Spring-Summer is defined as March through August (inclusive). Season thresholds should not be changed based on local conditions due to the empirical nature of the coefficients. Adapted from Albright et al. (2010).

Required storage on an annual time scale (S_r) is calculated by summing the positive monthly required storage for each month of a given year (ΔS_i, for i months), as given by equation 6:

$$S_r = \sum_{i=1}^{12} \Delta S_i \text{ for } \Delta S \geq 0 \tag{6}$$

The resulting S_r from equation 6 can then be substituted into equation 3 to solve for the required cover thickness given the local soil characteristics and meteorological conditions of the chosen year of data.

In practice, Albright et al. recommend performing several iterations of the calculations with different years of data. The authors recommend starting with historical annual cumulative precipitation data for a range of years, finding the "typical" (average) year and 95th percentile year based on annual cumulative precipitation, and then performing the calculations described above. This methodology provides two data points for plausible conditions and for what would be expected in a more extreme precipitation year. Depending on the goal of the ET cover, different percentiles or thresholds could be calculated to determine the approximate cover thickness. It is critical to note that different use cases for ET covers have variable thresholds for percolation. In many landfill situations such as the book is written for, a small amount of percolation may be allowable. In the context of biomass burial, our model is designed to have zero percolation. Albright et al. emphasize that this is preliminary modeling and that a more robust and detailed water balance model such as HYDRUS-1D or UNSAT-H should be used before burying waste with an ET cover (Fayer, 2000; Simunek et al., 2005). However, the method still stands as a conservative theoretical framework for the required cover thickness, and thus can be adapted to our geospatial approach.

2.2.2 Introduction to Applied Water and Input Data

The goal of this work is to build a geospatial tool hosted in ArcGIS to inform regions of interest for woody biomass burial. As such, all input data must be geospatial in nature. Given the simplified, empirical equation for required storage presented by Albright et al. (Equation 5) and the soil data requirements of the required cover thickness (Equation 3), the most basic approach requires the following data: volumetric soil water content at field capacity (θ_c), volumetric soil water content at wilting point (θ_m), total monthly precipitation (P), and total monthly potential evapotranspiration (PET). The soil parameters, volumetric soil water content at field capacity and wilting point, are commonly measured in soil sampling. On a geospatial basis, these parameters, among many other soil properties, are characterized on a 30 m by 30 m basis for each soil horizon across the United States in the gridded National Soil Survey Geographic Database (gNATSGO) from the Natural Resources Conservation Service within the U.S. Department of Agriculture (USDA)(Soil Survey Staff, 2023). The gNATSGO database was retrieved in February 2024. We assume that the soil types and distributions have not and will not change significantly on decadal scales (Jackson and Overpeck, 2000). Additionally, this analysis assumes that soil structure and composition are not altered from pre-disturbance conditions, and the cover is not engineered. Further discussion of soils is out of scope for this thesis, but soil properties and characteristics influence burial potential and should be considered.

Required storage requires precipitation and PET input data. Equation 5 uses a parameter, β, multiplied by PET to approximate the actual evapotranspiration, AET, since PET can be calculated from common meteorological data and AET is challenging to measure. However, since historical AET data is available from remote sensing and model-based products, and it represents a more accurate description of a location's water balance, we chose to use AET instead of the β-coefficient approximation method. The Operational Simplified Surface Energy Balance (SSEBop) model, version 6 (V6) has a global AET output with a 1 km by 1 km resolution (Senay and Kagone, 2019). The SSEBop modeling approach combines remote sensing data from Landsat and MODIS satellites with a reference ET derived from climatological datasets in a model to calculate actual evapotranspiration (Senay et al., 2013, 2022). The monthly cumulative AET product was used in versions 1 and 2 of required cover thickness presented here, and the temporal range of data availability from 2013 to 2022 initially constrained the years we used for historical climate data in monthly applications. At the beginning of 2024, daily SSEBop V6 data was published, and daily AET was retrieved for 2000 to 2021 for the daily water balance implementation for version 3 of required cover depth.

Climatological data was acquired from the Daymet, version 4.1 (V4.1) data product which provides daily surface weather records at a 1 km by 1 km spatial resolution from 1980 to near-present for North America and U.S. territories (Thornton et al. 2022). Daymet performs quality control on weather station data from the Global Historical Climate Network Daily database (GHCNd) and spatially interpolates the cleaned data with an algorithm trained for the Western US (Thornton et al. 2021). The primary output variables are daily maximum temperature (T_{max}), minimum temperature (T_{min}), and total precipitation (P, denoted $Prcp$ in Daymet documentation). Additionally, Daymet calculates snow water equivalent (SWE), daily average water vapor pressure (VP), daylight average shortwave radiation ($Srad$), and daylength ($Dayl$). All Daymet V4.1 data was acquired as multi-dimensional arrays (netCDFs) using the Python package, Pydaymet, which allows users to easily acquire several variables in the same file and clip the geospatial extent to a shapefile (Chegini et al., 2021).

While Daymet provides daily precipitation data, precipitation alone does not temporally account for when the water in precipitation will reach the soil column if the precipitation falls as snow. Much of the Western U.S. receives winter snow, and snow accumulation and ablation serve to shift the temporal distribution of when water is delivered to the soil surface by storing the moisture aboveground for a period of time (Stewart, 2008; Trujillo and Molotch, 2014). Preliminary data analysis suggested that this phenomenon could results in over 100 mm of water being stored through the winter and applied in a springtime pulse in some regions, particularly in places with high topography. This is not accounted for in the simple equation 5.

As such, we decided to move to an applied water approach instead of relying on precipitation. Applied water describes the water that reaches the atmosphere/soil surface on a given day. Water content reaching the soil profile from snowpack is most conservatively estimated by ignoring sublimation, surface liquid evaporation, and wind transport, which cannot be geospatially determined due to the highly heterogeneous and variable nature of these factors (Svoma, 2016). In its most simple formulation, applied water can be described as the sum of rainfall and snowmelt for a given day.

Two methods of calculating applied water are presented in this thesis. Briefly, an initial approach based on the Daymet snow water equivalent (SWE) product is discussed in section 2.2.3 but found to be faulty due to the lack of mass balance in the underlying SWE model. An updated, more sophisticated approach based dependent on temperature and solar radiation is discussed in the following sections for the remainder of the versions (Section 2.2.4). All calculations were performed in Python with the exception of some calculations in early versions noted in ArcGIS Pro. The open-source Xarray package was used extensively to manipulate the multi-dimensional arrays (Hoyer and Hamman, 2017).

All versions are based on an adaptation the ET cover depth estimation methodology from Albright et al. (2010) for geospatial application across the Western US. We adapted the required storage formula, equation 5, given the available AET data and use of applied water, resulting in the following equation for soil water balance,

$$\Delta S = AW - AET \tag{7}$$

where AW is applied water and AET is actual evapotranspiration, both in units of mm. For the first two versions discussed here, soil water balance is performed on a monthly scale, and thus applied water and AET are accumulated into monthly totals. In version 3, daily water balance is used. The loss term, Λ, from the original equation 5 is ignored to have a more conservative estimate that assumes all water that reaches the surface moves vertically downward. Annual required storage (S_r) is calculated as described by equation 6 when equation 7 is implemented on a monthly basis.

2.2.3 Required Cover Thickness, V1: Monthly Applied Water Derived from a Daymet SWE-based Snow Model

The first iteration of the applied water model used the precipitation and snow water equivalent (SWE) products from Daymet to calculate daily rainfall and snowmelt, which were summed to calculate daily applied water and then aggregated on a monthly basis. Precipitation in Daymet describes the depth of liquid water that falls over the course of a given day (mm d^{-1}), regardless of if it fell as rain, snow, or, more rarely, other forms of precipitation such as hail. SWE is a cumulative metric that describes the mass of water stored in the snowpack over a given area in the units of kg m^{-2}. When precipitation falls as snow, SWE increases. SWE decreases as snow melts.

Daymet utilizes a simple accumulation and melt algorithm to generate SWE from the primary Daymet variables, and this method is described across several publications. Snow is accumulated if precipitation falls when the daily average temperature is less than 0.0ºC (Thornton et al. 2000). The accumulation condition for a given day is as follows:

$$SA = P \text{ when } \frac{T_{max}+T_{min}}{2.0} < 0.0℃ \quad (8)$$

where SA is snow accumulation in terms of liquid water depth (mm d^{-1}), P is precipitation (mm d^{-1}), T_{max} is maximum daily temperature (ºC), and T_{min} is the minimum daily temperature (ºC). The variables P, T_{max}, and T_{min} are all primary variables in Daymet. From this accumulation condition, we can infer that for a precipitation event on a given day associated with an increase in SWE on a given day, snow accumulation in liquid units can be converted to SWE using the density of water, which is reasonably approximated in Daymet as ρ_w = 1000 kg m^{-3}:

$$\Delta SWE_{+} = SA * \rho_w \tag{9}$$

According to the recently published Daymet V4 documentation (Thornton et al., 2021), the methodology for Daymet SWE is based on the Thornton et al. (2000) paper. Thornton et al. (2000) describes a water vapor pressure and shortwave radiation joint retrieval developed and calibrated in the Austrian Alps. In this paper, snowmelt is calculated on a daily timestep according to a calibrated rate when the minimum temperature is greater than a calibrated critical temperature threshold, following the methodology presented in Running and Coughlan (1988). The calibration of this snowmelt rate and critical threshold for snowmelt is not described in the most recent citing literature (Thornton et al., 2021), and the only values presented within all the citing literature are calibrated for the three sites in the Austrian Alps as described by Thornton et al. (2000). This ambiguity became a major concern and partially drove the decision for developing a different applied water model, as described in later sections. Given the published information, the snowmelt equation for the Daymet SWE product appears to be as follows (Thornton et al., 2000):

$$SM = r_m * \frac{(T_{min} + T_{max})}{2.0} \text{ when } T_{min} > T_{crit} \tag{10}$$

where SM is snowmelt (mm d^{-1}), r_m is the calibrated melt rate (mm ºC^{-1} d^{-1}), and T_{crit} is the calibrated critical temperature (ºC). The values cited for the Austrian Alps in Thornton et al. (2000) for r_m and T_{crit} were 0.420 mm ºC^{-1} d^{-1} and -6.0 ºC, respectively. It remains unclear whether these calibrated values are used for the North American Daymet domain despite a careful literature review and attempts to contact the Daymet technical team. Regardless of the specific values, SWE would decrease for a given day by the mass per unit area equivalent of snowmelt using the density of water conversion:

$$\Delta SWE_{-} = SM * \rho_w \tag{11}$$

The Daymet variables precipitation and SWE can be used to develop a simple logic model to calculate applied water. For a given day, rainfall is defined as precipitation that falls when the average of the minimum and maximum temperature is greater than 0.0ºC, and snowmelt is defined as the negative change in SWE converted to the water depth equivalent (Figure 1). In the logic model developed here, if precipitation falls on a given day when the temperature-based accumulation condition is not met, it is recorded as rainfall (RF) in units of mm d^{-1}:

$$RF = P \text{ when } \frac{T_{max}+T_{min}}{2.0} > 0.0°\mathrm{C} \tag{12}$$

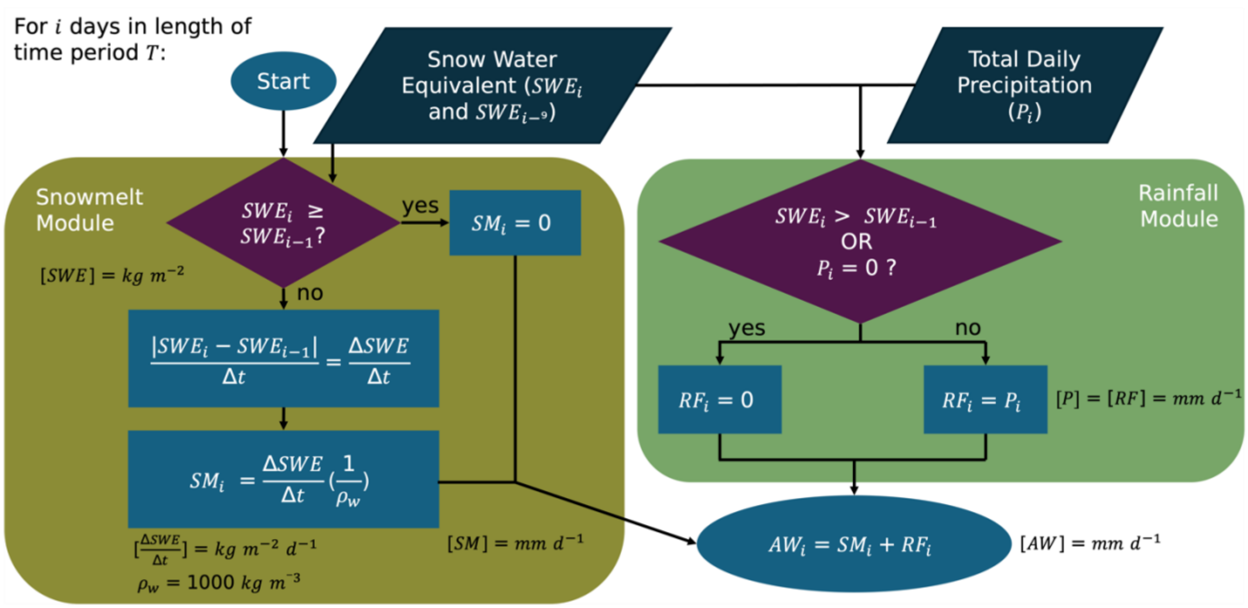

Figure 1: The initial logic model for applied water based on Daymet daily total precipitation and SWE. In the snowmelt module, if SWE for a given day is greater than or equal to SWE on the prior day, snowmelt is set to zero. If SWE for a given day is less than SWE on the prior day, the change in SWE is converted using density to snowmelt in units of mm d^{-1}. In the rainfall module, if SWE for a given day is greater than for the prior day or precipitation is equal to zero, rainfall is set to zero. If SWE for a given day is not greater than the prior day and precipitation is not equal to zero, the total daily precipitation is recorded as rainfall. Rainfall and snowmelt for a given day are summed to calculate applied water for a given day. Once daily applied water is calculated for each day, it is summed into a monthly cumulative timestep.

Given the ambiguity of the snowmelt algorithm in SWE as described above, snowmelt (SM) was defined in the model as the negative change in SWE from the prior day to the current day, divided by the density of water with final units of mm d^{-1} (equation 13).

$$SM_i = \frac{|SWE_i - SWE_{i-1}|}{\Delta t * \rho_w} \text{ when } SWE_i < SWE_{i-1} \tag{13}$$

where i represents the current day, $i-1$ represents the day prior, and Δt represents the time step between i and $i-1$ (assumed to be 1 day). Applied water (AW) for a given day can be described simply as the sum of rainfall and snowmelt for that day, all in units of mm d^{-1}.

$$AW_i = RF_i + SM_i \tag{14}$$

Once daily applied water is calculated for all days within the time period 2013-2022, it is summed into a monthly timestep for this time period. This temporal resolution both matches the inputs for the required water storage equation 7 from Albright et al. (2010) while retaining resolution of seasonal changes with a far smaller amount of data relative to daily resolution.

Daymet has a monthly total precipitation product available for direct download, and this is adequate to describe total precipitation in version 1 since it is a simple sum of daily precipitation over a monthly timestep. Daymet also offers an average monthly SWE product, but average monthly SWE does not account for the daily fluctuations of snow accumulation and snowmelt. In short, snowmelt is path-dependent and cannot be derived from a monthly average value. Since snow accumulation and melt calculations require both SWE and preciptitation, both daily SWE and daily precipitation must be acquired and processed. Daily snowmelt can then be summed for each day.

The implementation of this logic model on a geospatial basis with daily precipitation and SWE was a significant computational challenge compared to previous modeling that could be completed in ArcGIS Pro. This required daily precipitation and SWE rasters for the Western

U.S. region for the 10 years of study, 2013-2022. To overcome the barrier of processing this data using a visual interface such as ArcGIS Pro, I wrote and implemented a Python script that calculated applied water on a daily basis. This daily applied water was then summed monthly for monthly cumulative applied water for the entire study region for one year at a time. Once monthly cumulative applied water was derived for each year between 2013-2022, it was averaged by month (i.e., every January averaged together) to create 12 individual rasters representing each month of average applied water over the 2013-2022 time period. Standard deviation and coefficient of variation (standard deviation divided by mean for each pixel) for each month were also calculated. These applied water rasters were then used with the average monthly cumulative AET rasters in equation 7 to calculate monthly required water storage (ΔS) in ArcGIS Pro. The result of equation 7 for each month was summed according to equation 6 to find the required storage (s_r), and the required storage along with the soil parameters for each pixel were used to calculate the required cover thickness (L) as described by equation 3. The resulting geospatial raster is V1 of required cover thickness.

However, the approach for calculating applied water from Daymet SWE presented here was not used in future versions of the model. Ambiguity within the Daymet snowmelt methods was described above, and I identified more concerns when checking the Daymet SWE algorithm for mass balance. When checking for mass conservation between the input precipitation and output applied water, I found that applied water represented more water mass than the precipitation input. The issue was not within the applied water logic model described here, however. The issue was identified within Daymet itself. For a majority of years in locations that have snow in the winter, there were SWE values on January 1st of a given year with no corresponding precipitation event in the given or prior year. Essentially, there was snowpack that appeared without a precipitation event, and SWE was discontinuous interannually. I reached out to the Daymet technical team with this concern several times with no response. The latest Daymet V4 data description paper states, “We encourage researchers who require a more accurate estimate of snowpack dynamics to use the temperature, precipitation, and potentially radiation and humidity variables from Daymet v4 to drive a more capable and sophisticated snow process model,” and acknowledges its model is “very simple” with the “sole purpose … to provide an approximate control on *Srad* through the multiple reflection mechanism” (Thornton et al. 2021). However, this very simple model should, in theory, be sufficient for basic applications such as ET covers, and several papers have been published based on Daymet SWE (e.g., Broberg, 2021). This disclaimer is not presented on the Oak Ridge National Laboratory Distributed Active Archive Center (ORNL DAAC) webpage where the Daymet data is acquired. Even if the model is simple, the published data should be algorithmically robust enough to have some utility, but it does not appear to be sufficient for any analysis. As such, I developed a new simple snow model to calculate applied water on a geospatial scale.

2.2.4 Required Cover Thickness, V2: Monthly Applied Water Derived from a Restricted Degree-Day Radiation Snowmelt Model

Due to the shortcomings described above, a new snowmelt model was implemented for the second version of applied water (Figure 2). The same methodology for determining rainfall as precipitation that fell when the average of minimum and maximum daily temperature was greater than 0.0ºC (Equation 8), and applied water as the sum of rainfall and snowmelt was retained in this version (Equation 14). After reviewing possible snowmelt algorithms and their computational intensity, the restricted degree-day radiation (RDDR) balance approach described by Kustas et al. was selected (1994). With the restricted degree-day radiation balance approach, snowmelt is calculated as follows:

$$SM = a_r T_d + m_Q R_n \text{ when } T_d = \frac{T_{max}+T_{min}}{2} > 0.0°\text{C} \tag{15}$$

where a_r is a restricted degree-day factor (mm ºC^{-1}), T_d is the degree-day temperature above a base temperature (considered to be 0.0ºC for this study), m_Q is a conversion factor from energy flux density to snowmelt depth (2.6 mm m^2 d^{-1} W^{-1}), and R_n is net radiation (W m^{-2}). The restricted degree-day factor, a_r, ranges from 2.0 – 2.5 mm ºC^{-1} with lower values corresponding to days with lower wind speeds or lower humidity which reduce sensible heat transfer or increase latent heat dissipation respectively (Martinec 1989). Given the relatively small range of possible a_r values and widespread of conditions, an average restricted degree-day factor of 2.25 mm ºC^{-1} was used. Since snow can be approximated as a blackbody for longwave radiation (Curley et al., 2014), net radiation (R_n) was calculated using daylight average shortwave radiation total transmittance ($Srad$, units W m^{-2}) from Daymet. Daylength ($Dayl$, units s) from Daymet was used to weight $Srad$ by daylength to calculate daily shortwave radiation total transmittance, and average snow albedo (α) was used to calculate net radiation, as shown in equation 16.

$$R_n = (\frac{Dayl}{86400\ s})(1-\alpha)(Srad) \tag{16}$$

We defined average snow albedo (α) as 0.74, which has been approximated as the average snow albedo between fresh snow and nearly ablated snow (Kustas et al., 1994; Khire et al., 1997).

To calculate snowmelt, snow must first be accumulated and stored in a reservoir. Snow was accumulated from precipitation in Daymet on a daily timestep using the same temperature-based accumulation condition described in equation 8. Snow water depth (mm) from the accumulation condition was converted using the density of water into snow water equivalent (SWE, units kg m^{-2}). SWE was constructed as a reservoir in the model where snow accumulation resulted in a flux into the reservoir and snowmelt resulted in a flux out of the reservoir. This required a daily iterative approach to account for snow accumulation, changes in snowpack storage, and snowmelt. Additionally, SWE storage from the final day of each year was stored and used to initialize the following year to ensure continuity in snowpack interannually. As with the previous version, daily rainfall and snowmelt were summed for daily applied water (Figure 2).

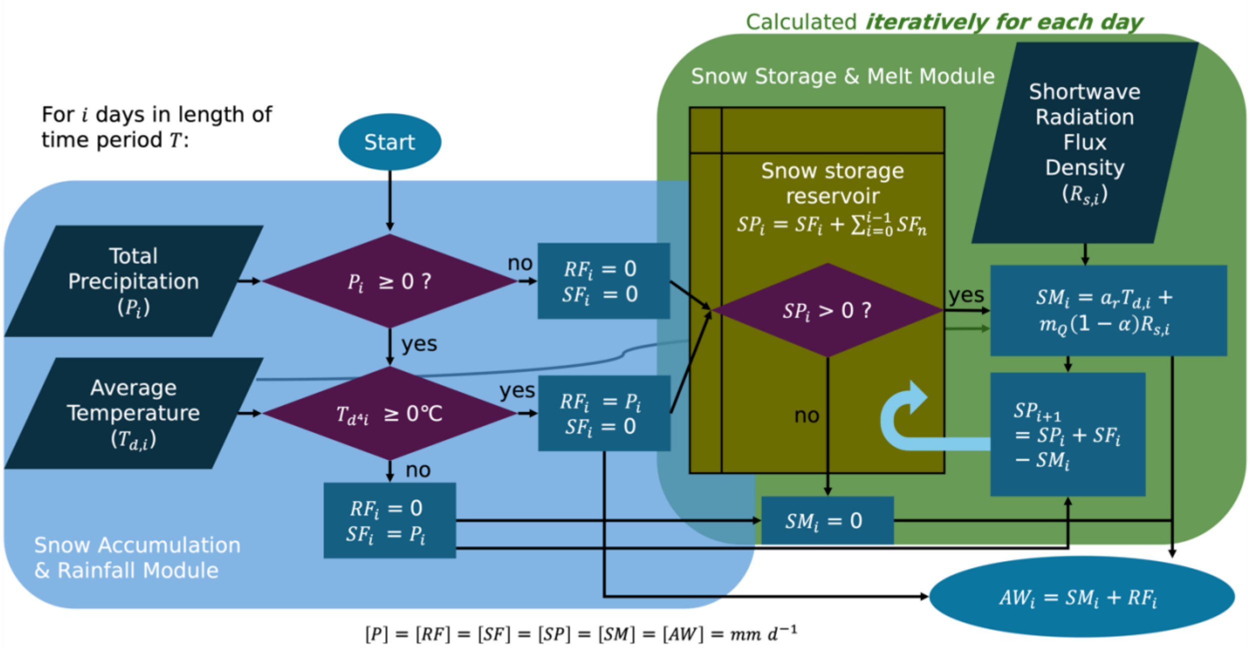

Figure 2: The logic model for applied water calculated using the restricted degree-day radiation (RDDR) snowmelt model approach. Daily total precipitation and average temperature are used to partition rainfall and snowfall. Water in snowfall is stored in a reservoir where the RDDR snowmelt equation is used with inputs of temperature and radiation to determine daily snowmelt. The snow storage reservoir is calculated iteratively for every day in the time series, where the stored snowpack from prior days is available for snowmelt on a given day, and the amount of snow accumulated or melted on a given day informs the initial snow storage reservoir size for the following day.

Computationally, this approach required over twice as much data for inputs as well as daily iterative computation over all 1.7 million pixels included in the Daymet swath of the Western US. As such, this model was designed for and run on Grace High Performance

Computing (HPC) using Python. With the higher computing power, I also ran a full year of data, 2012, to initialize the snow storage reservoir for the 10-year time series from 2013-2022.

As described in the first version of applied water, daily applied water was aggregated into monthly products. Once monthly cumulative applied water was derived for each year between 2013-2022, it was averaged by month (i.e., every January averaged together) to create 12 individual rasters representing each month of average applied water over the 2013-2022 time period. Standard deviation and coefficient of variation for each month were also calculated. These applied water rasters were then used with the average monthly cumulative AET rasters in equation 7 to calculate monthly required water storage (ΔS) in Python. The result of equation 7 for each month was summed according to equation 6 to find the required storage (s_r), and the required storage along with the soil parameters for each pixel were used to calculate the required cover thickness (L) as described by equation 3. The resulting geospatial raster is V2 of required cover thickness.

2.2.5 Required Cover Thickness, V3: Daily Water Balance Modeling using the RDDR Applied Water Approach

Given the coarse temporal resolution in the monthly water balance approximations presented in V1 and V2, with the publication of daily AET data in early 2024, we developed V3 of the burial tool using a daily water balance for 2001-2020, with 2000 as an initialization year. In V1 and V, annual aggregation through monthly averaging dampened the influence of extreme precipitation events on the calculated applied water, but understanding maximum storage requirements is critical in required depth calculations. Additionally, the probability density functions of applied water events and their magnitudes are heavily skewed to the right, so high applied water days are few but very impactful. Further, it is critical to understand AET relative to applied water at a final temporal resolution than the accumulated monthly data. A string of cold, cloudy wet days when evapotranspiration is low could result in large amounts of water reaching the soil column, yet this mismatch between applied water and precipitation may be washed out on the monthly scale. Thus, I updated V2 of the model to utilize daily applied water and AET in an accumulated required water storage approach to understand the amount of water that the soil could have to store on any given day.

Applied water was calculated as outlined in the V2 model section (section 2.2.4) using the RDDR approach for snowmelt. The only change in methodology was that the data was kept at a daily resolution and not aggregated to cumulative monthly totals. The temporal range was selected to match the availability of AET data. All annual applied water netCDFs containing daily data for all years 2000-2021 were merged into one continuous netCDF to allow for continuous iterative calculation of water balance.

Daily AET rasters from SSEBop were retrieved from the USGS archive using a batch download script in Python. Each daily GeoTIFF raster was reprojected from WGS84 to North American Lambert Conformal Conic to match Daymet data using cubic convolution. Each reprojected GeoTIFF was then clipped to the geographic extent of the applied water data and built into a netCDF using GDAL and Xarray libraries in Python. Cubic convolution was chosen for its ability to preserve extrema. All daily netCDFs were compiled into one continuous netCDF along the time axis for 2000 to 2021. December 31st on leap years was removed following the Daymet convention to match the applied water time indexing. The resulting AET netCDF had the same time indexing and geospatial pixel size and dimensions as the applied water netCDF which allowed for calculation across the two files.

Instead of a traditional mass balance equation that assessed the change in water stored in the column, the daily water balance model was designed to understand the amount of storage required, in units of liquid water depth, under the assumption that there was no percolation from the soil layer to stored biomass. This daily water balance was calculated using an iterative approach with applied water and AET fluxes relative to an unconstrained water storage reservoir. Simply, the model assumed that for any given day, water could be added to the storage reservoir from applied water or removed by AET. For the first day in the time series, the required storage, $s_{r,0}$, was equal to applied water minus AET (Equation 17; zero index to follow the Python convention). If applied water exceeded AET for any given day i in the time series, the amount of water not evapotranspired would be added to the reservoir. Water within the reservoir is carried over each day and only removed if there is an excess of AET greater than applied water on a given day. The reservoir can deplete to a minimum of 0, but there is no bound on the upper limit of the reservoir. Daily required storage ($s_{r,i}$) for the first day and all subsequent days is described in equations 17 and 18, respectively:

$$s_{r,i} = AW_i - AET_i \text{ for } i = 0 \tag{17}$$

$$s_{r,i} = s_{r,i-1} + AW_i - AET_i \text{ for } i > 0 \text{ and } s_{r,i-1} > 0 \tag{18}$$

If $s_{r,i}$ for a given day is less than zero, it is recorded as zero since negative water storage is not possible but instead is indicative of no required water storage in the soil column. Daily required storage was calculated for each pixel on each day of the time series iteratively and stored in a new netCDF with the same geospatial and time dimensions as the input data. After the iterative daily calculations were complete, the initialization year, 2000, was cut from the dataset. In agricultural systems, water that is not precipitation may be applied to fields, thus resulting in a higher observed AET from the USGS product which is reliant on remote sensing data. This would result in erroneously low required water storage. Pixels classified as waterbodies, wetlands, or agricultural were masked using the National Land Cover Database (NLCD) (Homer et al., 2012).

For daily required water storage, we calculated several statistics to describe the distribution of required storage. Mean and standard deviation were calculated for each pixel across all days in the final required storage record. Coefficient of variation was calculated by dividing standard deviation by the mean for each pixel to understand the variability relative to the mean magnitude. Median, 95th percentile, and maximum required storage were retrieved for each pixel. Ninety-fifth percentile required water storage ($s_{r,95}$) and maximum required storage ($s_{r,max}$) were used to calculate required cover thickness following equation 3. Given the assumptions in our model, as described below, 95th percentile required storage is likely a more reasonable approximation of actual required storage, but we present the results of the maximum required water storage as well. The resulting required cover thickness raster is termed V3.

2.2.6 Model Assumptions

In order to build an extensive geospatial model covering variable terrain, we employed several assumptions to simplify the model. For each assumption we made, we were careful to ensure that the assumption made our model more conservative (i.e., predicting higher required water storage resulting in a greater required cover thickness). We assume that all water received as precipitation to a given pixel vertically infiltrated the soil column of that pixel. We did not exclude precipitation that was intercepted by plant or other aboveground material and evaporated back to the atmosphere without reaching the soil column. Runoff was not considered. Snow sublimation, snow transport via wind, and mass gain or loss from water vapor interacting with snowpack were not modeled.

2.2.7 Statistical Analysis

Descriptive statistics for input variables were assessed using probability density functions (PDFs) to understand the distribution of observations. We calculated basic descriptive statistics, mean, standard deviation, and coefficient of variation, for each iteration of the resulting required water storage or minimum cover thickness.

2.3 Results

Monthly model V1 produced the results shown in figure 3. Required cover thickness is highest along the Pacific Northwest coast in Washington, Oregon, and Northern California, and in the mountain ranges including the Cascades, Sierra Nevada, and Rockies and other points of high elevation. Required cover thickness is lowest in the Great Plains east of the Rockies, the warm deserts of New Mexico and Arizona, and some of the intermountain basins such as the Central Valley of California and basins in the Basin and Range region of Nevada and Utah. Modeled required cover thickness across the region of interest is as low as 0 m for both the model with and without SWE. Minimum required cover thickness with SWE has a mean of 3.4 m and standard deviation of 10.1 m (Figure 3a). Minimum required cover thickness without SWE has a mean of 2.4 m and a standard deviation of 8.7 m (Figure 3b). Required cover thickness when calculated with the monthly applied water model V1 is generally 0.25 m or less greater than required cover thickness calculated solely with monthly total precipitation without accounting for the distribution of SWE (Figure 3c). The modeled burial depth is 3 mm deeper on average across all pixels when applied water with SWE is used. There are a few pixels in the Sierra Nevada and Rockies where burial depth is up to 3 m deeper when snow is accounted for using SWE.

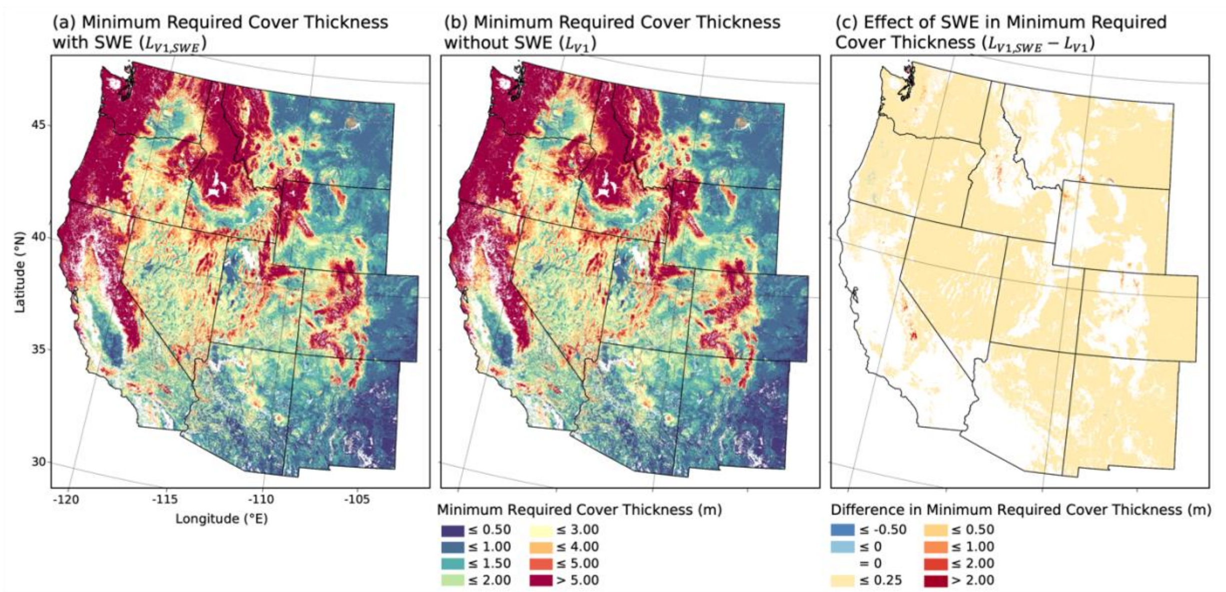

Figure 3: The minimum required cover thickness determined using (a) the applied water calculated from the V1 monthly SWE-based model and (b) monthly total precipitation directly from Daymet. (c) shows the difference between the modeled required cover thickness for each pixel.

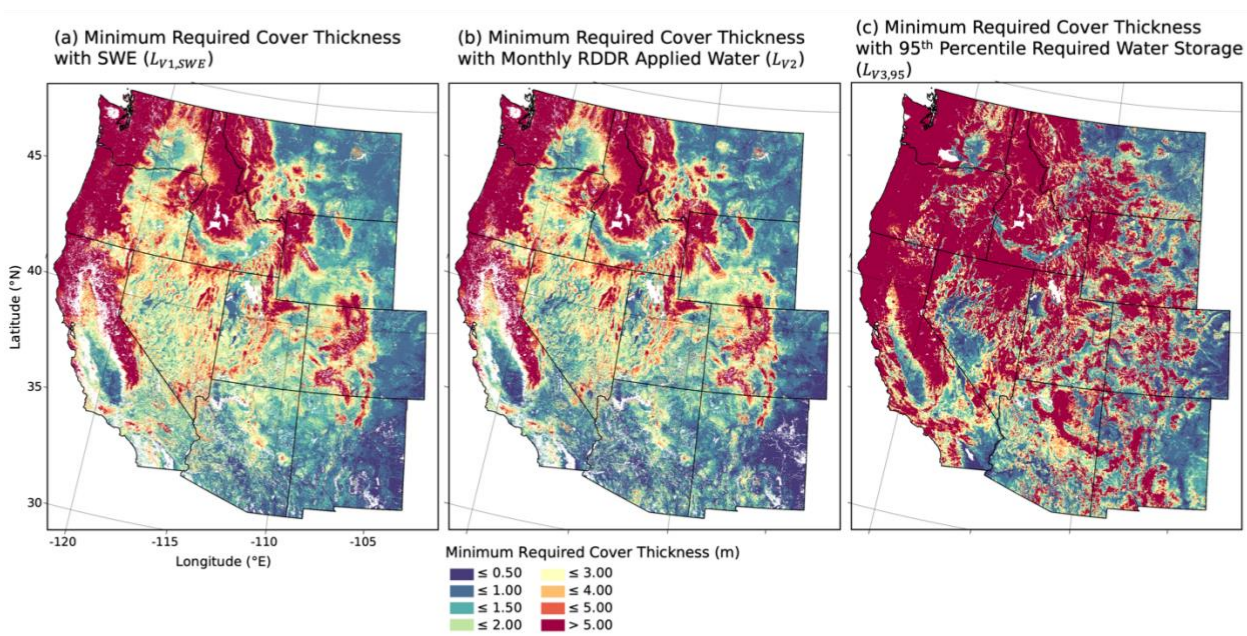

Figure 4: Minimum required cover thickness for model versions 1-3 (a-c). Panel (a) shows the minimum required cover thickness derived using monthly Daymet SWE-based applied water model (V1). Panel (b) shows the minimum required cover thickness using monthly applied water derived using the RDDR snowmelt model (V2). Panel (c) shows the minimum required cover thickness based on the 95th highest day of water required storage calculated from the daily accumulated water balance model (V3). Panels and (a) and (b) show the minimum required cover thickness using meteorological inputs from 2013-2022. Panel (c) uses meteorological inputs from 2001-2020. None of these panels are masked with the NLCD mask.

Version 2 of the minimum required cover thickness model based on monthly applied water calculated with the RDDR snowmelt approach has a very similar geospatial distribution to V1 (Figure 4a, b). The topographic high points and the Northern Pacific coast show higher required storage due to higher precipitation. Required cover thickness broadly decreases, with a geospatial average of 2.5 m with a standard deviation of 9.8 m.

Version 3 of the minimum required cover thickness model is based on the accumulated required water storage, as liquid water depth, determined by the water balance model. Mean, 95th percentile, and maximum accumulated required water storage are presented in figure 5 a, c-d. For all three levels of required water storage, the minimum required water storage is 0 mm, and the distribution of required water storage is skewed right. Since the model water storage reservoir has no size limit, the modeled maximum required water storage for any given pixel over the 2001-2020 period was 95.2 m of water. The geospatial average of mean daily accumulated required water storage ($\bar{s}_r$) was 0.93 m with a standard deviation of 2.8 m of water. For 95th percentile required water storage, the mean was 1.8 m with a standard deviation of 5.3 m of water. For maximum required water storage, the mean 1.9 m with a standard deviation of 5.7 m of water. Required water storage is highest in the Cascade mountains, the Sierra Nevada mountains, and along the Pacific Northwest coast. Required water storage is the lowest in the southern regions of California, Nevada, Arizona, and New Mexico and east of the Rockies in the Great Plains, as well as many of the topographic lows throughout the Western US. Coefficient of variation, the ratio between standard deviation and mean, is higher in these regions as well.

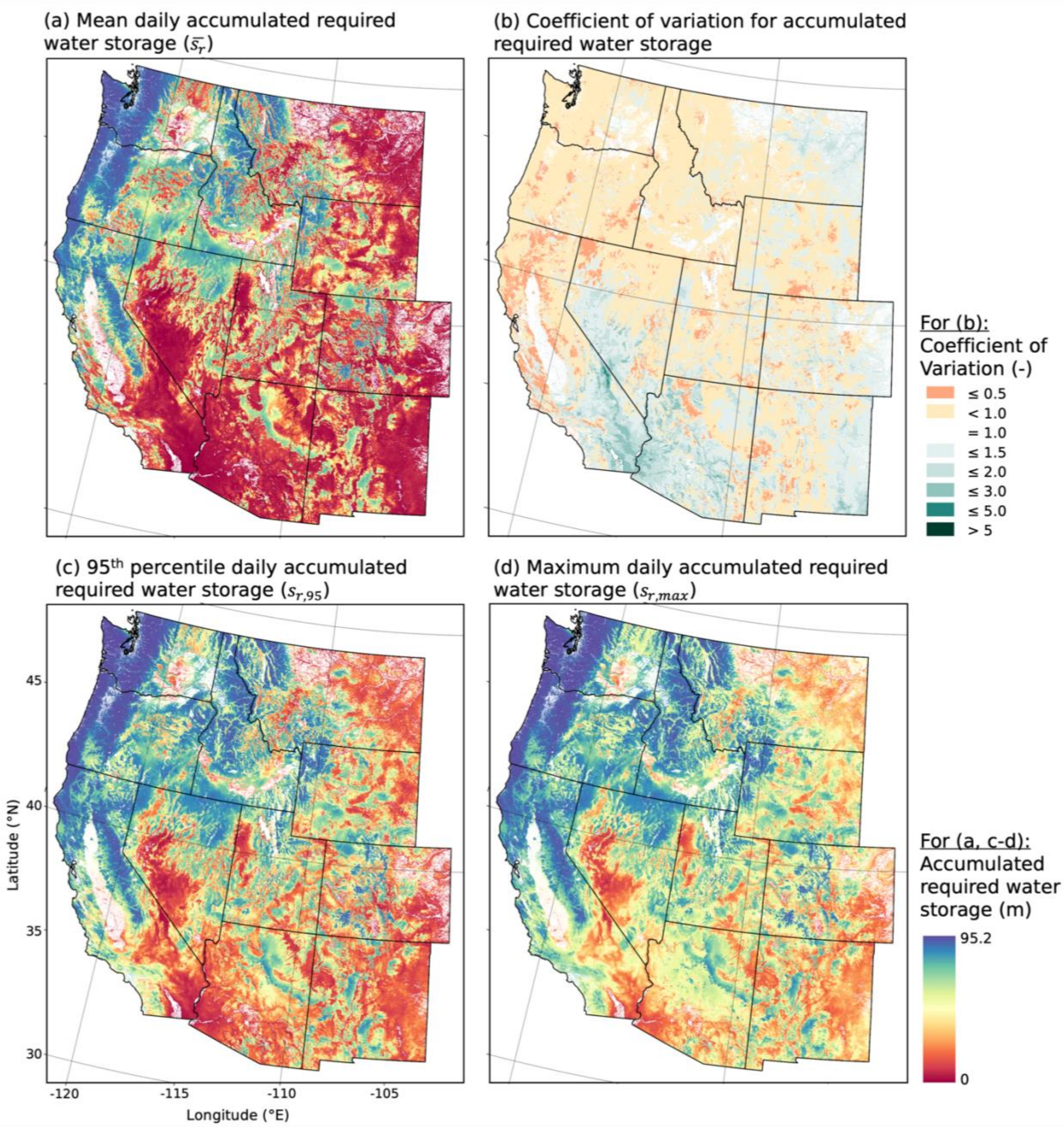

Figure 5: Daily accumulated required water storage for the Western US, 2001-2020, calculated using the RDDR snowmelt model applied water approach (V3). Pixels classified as waterbodies, wetlands, or agricultural lands using the NLCD are masked white. Panel (a) shows the mean daily accumulated required water storage ($\bar{s}_r$) for each pixel (time averaged over the 2001-2020 time period). Panel (b) shows the coefficient of variation for each pixel, where coefficient of variation is equal to the standard deviation of daily accumulated required water storage over the time period divided by the mean over that time period, $\bar{s}_r$. Panel (c) shows the 95th percentile highest daily accumulated required water storage during the 2001-2020 time period ($s_{r,95}$). Panel (d) displays the maximum daily accumulated required water storage during the 2001-2020 time period ($s_{r,95}$).

The required cover thickness from the modeled accumulated required water storage (V3) is presented in figure 6. As implicated by the calculation, maximum required water storage results in thicker required covers than 95th percentile required water storage. Compared to V1 and V2, V3 has a much higher fraction of the Western US with required cover thicknesses greater than 5 m. The geospatial average minimum required cover thickness with maximum required water storage ($L_{V3,max}$) is 15.9 m with a standard deviation of 53.6 m. The geospatial average minimum required cover thickness with 95th percentile required water storage ($L_{V3,95}$) is 14.7 m with a standard deviation of 51.0 m.

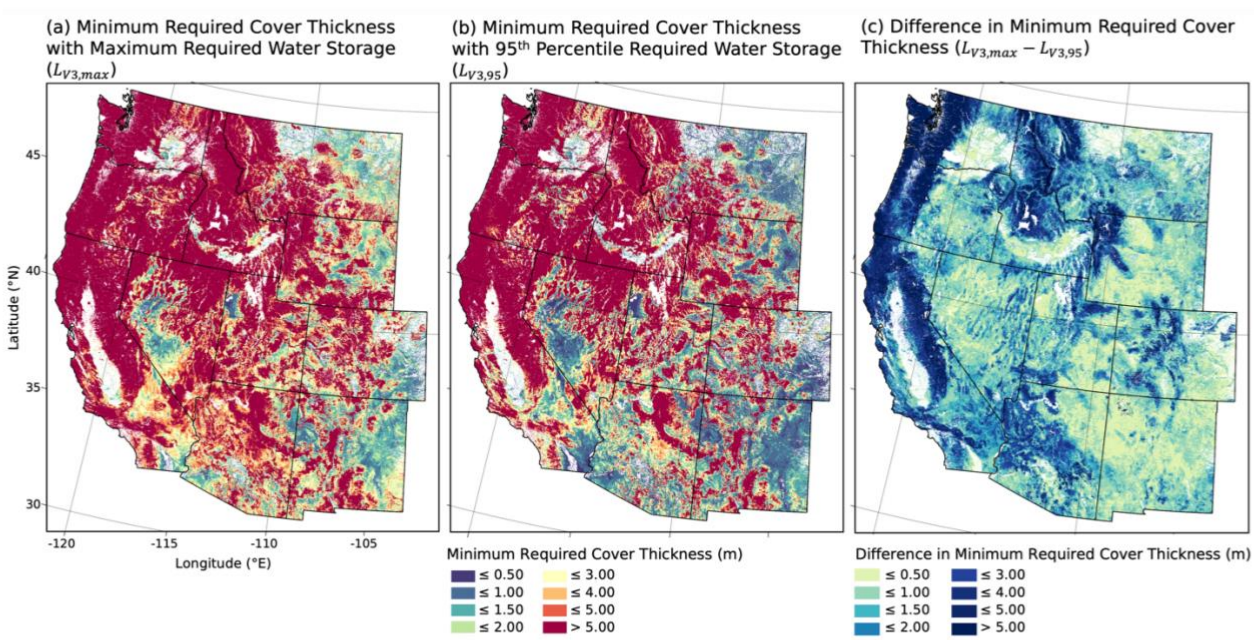

Figure 6: Minimum required cover thickness calculated from (a) maximum required water storage ($s_{r,max}$) and (b) 95th percentile required water storage ($s_{r,95}$) products from model V3 for the Western US, 2001-2020. Panel (c) shows the difference in the minimum required cover thickness between (a) and (b). White areas are masked.

2.4 Discussion

While V1 and V2 of minimum required cover thickness capture the broad trends in required cover thickness described in V3, far more assumptions are used and the coarse timestep (monthly) decreases our confidence in the numerical output from those models. In comparison, V3 utilizes a daily water balance approach based on applied water, AET, and water storage where the finer temporal resolution captures the variability of applied water and evapotranspirative demand relative to each other. Version 3 realistically models snow dynamics within daily applied water, and the daily SSEBop product has been verified to provide reasonable quantifications of AET (Senay et al., 2022). As such, we have confidence that the minimum required cover thickness derived from V3 of the modeling represents the most plausible first approximation of what regions may be most suitable to woody biomass burial. Given the issues described in the methods section with the Daymet SWE product, we have very low confidence in the results quantifying the effect of SWE on required cover thickness in V1. Version 3 indicates that V1 and V2 under-predict minimum required cover thickness and as such, over-predicts regions that may be suitable to biomass burial.

In the Western US, western Nevada, the Sonoran Desert, parts of the Colorado Plateau in the Four Corners region, and the Great Plains have the highest potential for woody biomass burial as indicated by the lowest required cover thicknesses. Regions of high topography, especially in the Pacific Northwest, appear poorly suited to woody biomass burial due to the high, and potentially extreme, amounts of required water storage. Geospatially, there are high standard deviations for required cover thickness within each product, indicating that there is significant variability across sites.

The geospatial implementation of simple water balance modeling across a broad region was only possible with the use of certain simplifying assumptions regarding runoff, snow sublimation, and wind transport of snow. We want to explicitly acknowledge that these assumptions may be more accurate for some regions or conditions than others. All modeling described here should at the very least be checked using local, site-specific data. Intensive climatologic, hydrologic, geologic, and pedologic modeling or experimentation should be undertaken before biomass burial is considered at a given site, for factors both included in our modeling and excluded due to the geospatial nature of our approach. Runoff was not included, and this assumption is reasonable in relatively flat areas. This assumption is likely less reasonable in steeply sloped terrain or terrain with a shallow depth to bedrock, but the constraints of biomass burial likely exclude these locations regardless. Runoff is dependent on the soil type and structure, presence of a frost line or frozen soil, and the slope, among precipitation factors such as precipitation intensity. Snow sublimation can be extensive, with up to 50% of snowpack being sublimated in some locations, but it is highly variable and at many sites, only a few percent of the snowpack is sublimated (Phillips 2013; Evans et al. 2016). Micro and macro-scale factors affecting sublimation have not been adequately parameterized for modeling across complex terrain and large spatial scales (Svoma 2015). Air temperature, humidity, wind speed, solar radiation, and ground cover can and should be used on a site-level basis to understand the impact of snow sublimation, transport via wind, and mass gain or loss from water vapor (Schmidt and Gluns 1992; Kampf et al. 2022). All assumptions, to the greatest degree possible, were chosen to make the resulting required cover thickness more conservative.

2.5 Conclusion

We successfully used publicly available meteorological data from Daymet and SSEBop to make a reasonable geospatial water balance product in V3 of required water storage. The results of this water balance were used to calculate minimum required cover thickness across the Western US, and these results indicate that there is potential for woody biomass burial from a macroclimate perspective. There is still a strong need for site-specific modeling and verification of the climatological geospatial products as well many other factors that would affect woody biomass burial, ranging from geological considerations such as the depth to bedrock and subsurface hydrology to social, political, and economic concerns such as environmental justice and existent infrastructure.

3. Projecting Future Potential for Woody Biomass Burial: Using CMIP6 Data to Model Applied Water, Potential Evapotranspiration, and Aridity Index

3.1 Introduction

As demonstrated in the previous section, woody biomass burial appears feasible in specific regions across the Western US under historical conditions from 2001-2020, but any consideration of durable carbon storage needs to take into account potential future climate conditions. Actual evapotranspiration (AET) is crucial for the water balance described in the prior section, and AET has been shown to correlate well with decomposition (Parton et al., 2007; Adair et al., 2008). Critically, AET is an observed value determined by the climatic, hydrologic, ecologic, and pedologic conditions at a given point in time. In contrast, potential evapotranspiration (PET) can be directly calculated from meteorological data, often with a component of vegetation parameterization. Numerous definitions and over 50 methods to calculate potential evapotranspiration (PET) exist in published literature (Lu et al., 2005; McMahon et al., 2013). Here, we follow the convention of Dingman (1992) where PET is defined as ". . . the rate at which evapotranspiration would occur from a large area completely and uniformly covered with growing vegetation which has access to an unlimited supply of soil water, and without advection or heating." The selection of PET equation is dictated by the region of interest and aims of a given study (Lu et al., 2005).

Methods have been developed to approximate AET from potential evapotranspiration (PET), such as the Budyko-Fu curves or empirical calibration (Milly, 1984; Chowdhury, 1999; Peng et al., 2018). However, these methods are generally specific to a relatively homogenous region such as a watershed and require accurate parameterization to produce meaningful results (Yang et al., 2009; Li et al., 2013; Peng et al., 2018; Ajjur and Al-Ghamdi, 2021; Taheri et al., 2022). Additionally, they approximate AET on longer time scales, generally annually, which makes it challenging to observe the effects of short but extreme events. Over large, heterogeneous regions such as the Western US, the approximation of AET from PET would not be precise enough for use in water balance, and the use of PET on a daily timescale is more meaningful.

Estimates of PET can be derived under simulated conditions from global circulation model (GCM) datasets using a range of modeled climate variables such as air temperature, solar radiation, relative humidity, and surface wind (Kingston et al., 2009; Berg and Sheffield, 2019). GCMs have been developed to quantify the geophysical atmosphere, ocean, and climate dynamics in future time periods under different emissions scenarios. Emission scenarios are determined by the amount and timing of greenhouse gas emissions. The Intergovernmental Panel on Climate Change (IPCC) coupled model organizes coupled model intercomparison projects (CMIPs) such that many GCMs around the globe are run under the same forcing conditions representing the emission scenarios. These model outputs can be analyzed in multi-model ensembles to understand the range of predicted trajectories of climatic variables throughout time under specified emissions scenarios (Pierce et al., 2009).

CMIP6, the most recent intercomparison project, was published between 2019 and 2022. Emissions scenarios in CMIP6 are termed “shared socio-economic pathways” or SSPs. CMIP6 presents five SSPs representing very low (SSP1-1.9), low (SSP1-2.6), intermediate (SSP2-4.5), high (SSP3-7.0), and very high (SSP5-8.5) greenhouse gas emissions through the 21st century (IPCC, 2023). For each emissions scenario, the first number describes a set of socio-economic conditions related to population size, gross domestic product, and urbanization that correspond to the magnitude of greenhouse gas emissions (Riahi et al., 2017). The number after the dash indicates the amount of radiative forcing caused by greenhouse gas emissions expected by 2100 under that emissions scenario in units of W m^2 (ex., 8.5 W m^{-2} for SSP5-8.5). Each SSP corresponds to a global warming temperature threshold from the historical baseline to 2100. SSP1-1.9 limits warming to <1.5ºC with no or limited overshoot, SSP1-2.6 limits warming to 2.0ºC, SSP2-4.5 limits warming to 3.0ºC, SSP3-.70 limits warming to 4.0ºC, and warming under SSP5-8.5 exceeds 4.0ºC (IPCC, 2023).

The IPCC released climate change synthesis report AR6 in 2023 and utilized CMIP6 data in their analysis. Among many global findings, they identified that more extreme precipitation events and droughts, decreases in soil moisture, and increases in aridity and fire weather are likely to become more common in the Western US with climate change (IPCC, 2023). Further literature has predicted intensifying drought in the Western US (Cook et al., 2015). Currently, there are no products that model PET at a high resolution with parameterization specific to the Western US using CMIP6 data, but PET is important in projecting evaporative demand in the future. Improvements in the CMIP6 modeling techniques and the accuracy of the SSPs developed over the decade since CMIP5 simulations appear significant enough to warrant creating these evapotranspiration products (Li et al., 2021; Martel et al., 2022). Developing an understanding of the predicted changes in water balance in the Western US will be critical in expanding our understanding of the impact of climate change on soil water content, extreme precipitation events, droughts, and fire weather.

In this section, I develop a geospatial implementation of a PET model based on the Penman (1948) PET equation with parameterization specific to the Western US. I run this model, with a complete integration of the daily applied water model described in section 2.2.4, with input data from 26 GCMs from CMIP6 under two SSPs to project potential changes in PET over the future time period through 2100. Changes in PET relative to changes in precipitation can be interpreted to understand how potential for woody biomass burial may change in the Western US over the 21st century.

3.2 Methods

3.2.1 Input Data

Since the goal of the burial tool to assist in location selection for possible woody biomass burial deployments, we wanted to preserve as fine of spatial resolution as possible while maintaining meaningful results. We conducted a review of spatially downscaled data products with daily temporal frequencies as well as the HighResMIP experiments from CMIP6 and large ensemble simulation models. We selected the NASA Earth Exchange Global Daily Downscaled Projections (NEX-GDDP-CMIP6) dataset which includes 35 GCMs downscaled to 0.25º by 0.25º resolution on a common grid (Thrasher et al., 2022). This product was selected for it's fine resolution, inclusion of a large number of GCMs, and universal gridding across GCMs. The NASA NEX-GDDP-CMIP6 is downscaled using the bias-correction/spatial disaggregation (BCSD) method which is described in detail in Thrasher et al. (2012). The dataset includes outputs for the four most common SSPs: SSP1-2.6, SSP2-4.5, SSP3-7.0, and SSP5-8.5. However, not every SSP is available for every GCM or variable. SSP2-4.5 (intermediate emissions) and SSP5-8.5 (very high emissions) were most commonly available across models, and these SSPs are the most commonly used to describe a range of future outcomes.

We acquired daily average temperature, minimum temperature, maximum temperature, precipitation rate, downwelling shortwave radiation, near-surface wind, and near-surface relative humidity (Table 1) for 26 GCMs from the NASA NEX-GDDP-CMIP6 THREDDS server in February 2024. Precipitation rate was reacquired in March following the release of version 1.1.

This data is hereafter refered to simply as "CMIP6 data" unless otherwise specified. All models that contained the requisite data variables for SSP2-4.5 and SSP5-8.5, with one exception, were used to maximize the number of models in the ensemble, which accounts for 26 out of the 35 available models (Table 2). All analysis was originally performed with the GISS-E2-1-G model, but the historical simulation data for this model was unrealistic and out of the plausible range of variability. As such, we removed the GISS-E2-1-G model from the ensemble. All acquired data was clipped within a bounding box from 31 to 49ºN and 102 to 124.75ºW, encompassing all the contiguous US west of Colorado's eastern border. For each variable analysed, we calculated a multi-model ensemble by first calculating each variable all the way through for each timestep (daily, monthly, seasonally, and annually) for each of the 26 models and then averaging each model results across each corresponding timestep. Standard deviation and coefficient of variation for each variable was also calculated at each timestep.

Aside from CMIP6 climatological data, the PET calculations required surface elevation data. We used acquired the USGS National Map 3D Elevation Program (3DEP) data with a 100 meter resolution (USGS, 2019). This data was upscaled in ArcGIS Pro using cubic convolution to match the datum, projection, bounding box, and pixel size of the CMIP6 data. The raster data was saved as a NetCDF for use in PET calculations.

CF Variable Name	Description	Units
$\boldsymbol{hurs}$	Near-surface relative humidity	%
$\boldsymbol{pr}$	Mean of daily precipitation rate	kg m^{-2} s^{-1}
$\boldsymbol{rsds}$	Surface downwelling shortwave radiation	W m^{-2}
$\boldsymbol{sfcWind}$	Daily mean near-surface wind speed	m s^{-1}
$\boldsymbol{tas}$	Daily mean near-surface air temperature	K
$\boldsymbol{tasmax}$	Daily maximum near-surface air temperature	K
$\boldsymbol{tasmin}$	Daily minimum near-surface air temperature	K

Table 1: CMIP6 variables used in this analysis. CF variable name refers to the NetCDF Climate and Forecast (CF) metadata convention. Near-surface indicates the variable was modeled at a height 2 m above the ground surface with exception of $sfcWind$ which is modeled 10 m above the ground surface.

Model	In ensemble?	Reasoning if excluded, when applicable
ACCESS-CM2	Y	-
ACCESS-ESM1-5	Y	-
BCC-CSM2-MR	N	No relative humidity ($hurs$)
CanESM5	Y	-
CESM2	N	No minimum/maximum temperature ($tasmin/tasmax$)
CESM2-WACCM	N	No minimum/maximum temperature ($tasmin/tasmax$)
CMCC-CM2-SR5	Y	-
CMCC-ESM2	Y	-
CNRM-CM6-1	Y	-
CNRM-ESM2-1	Y	-
EC-Earth3	Y	-
EC-Earth3-Veg-LR	Y	-
FGOALS-g3	Y	-
GFDL-CM4 (gr1)	Y	-
GFDL-CM4 (gr2)	N	Identical results to GFDL-CM4 (gr1) on different grid
GFDL-ESM4	Y	-
GISS-E2-1-G	N	Historical simulation data erroneous
HadGEM3-GC31-LL	Y	-
HadGEM3-GC31-MM	N	No SSP2-4.5
IITM-ESM	N	No minimum/maximum temperature ($tasmin/tasmax$)
INM-CM4-8	Y	-
INM-CM5-0	Y	-
IPSL-CM6A-LR	Y	-
KACE-1-0-G	Y	-
KIOST-ESM	N	No relative humidity ($hurs$) for 2058, SSP2-4.5
MIROC-ES2L	Y	-
MIROC6	Y	-
MPI-ESM1-2-HR	Y	-
MPI-ESM1-2-LR	Y	-
MRI-ESM2-0	Y	-
NESM3	N	No relative humidity ($hurs$)
NorESM2-LM	Y	-
NorESM2-MM	Y	-
TaiESM1	Y	-
UKESM1-0-LL	Y	-

Table 2: CMIP6 models within the NASA NEX-GDDP-CMIP6 downscaled product with designations of if a given model was used in this analysis and the reasoning if the model is excluded. 'Y' denotes that the model was included while 'N' with red shading indicates that a model was excluded from the ensemble.

3.2.2 Adaptations of Applied Water for CMIP6 Data

The foundations for the daily applied water model for CMIP6 data were based on the historic applied water model with the restricted degree-day radiation (RDDR) snowmelt model described in detail in section 2.2.4. All equations, constants, and the theoretical basis remain the same, but several of the variables require unit conversion. Precipitation is provided from CMIP6 as the mean daily precipitation rate in units of kg m^{-2} s^{-1} (pr). To convert to daily total precipitation (P), we converted from mass per unit area to depth of water in mm using the density of water (ρ_w = 1000 kg m^{-3}) and multiplying by the length of the day in seconds (86400 seconds). Daily average temperature (tas) from CMIP6 was converted from Kelvin to degrees Celsius. Surface downwelling shortwave radiation ($rsds$) is given as the daily average in units of W m^{-2}, so no correction from were necessary, unlike with the daylight-average $srad$ variable from Daymet. The applied water model for CMIP6 data was directly integrated into the PET model described in section 3.2.3.

Although the NASA NEX-GDDP-CMIP6 data is downscaled and bias-corrected with historical data, we wanted to confirm that this output was compatible with historical Daymet applied water. The NASA NEX-GDDP-CMIP6 product uses the Global Meteorological Forcing Dataset (GMFD) for Land Surface Modeling from the Terrestrial Hydrology Research Group at Princeton University for historic climate data (Sheffield et al. 2006). For a historical test period of 2000-2014 with 1999 as an initialization year, we calculated the total cumulative applied water using both Daymet and NASA NEX-GDDP-CMIP6 historical experiments. The Daymet total cumulative applied water for 2000-2014 was upscaled and regridded using cubic convolution to match the datum, projection, and resolution of the CMIP6 data. We calculated the percent difference between the Daymet and CMIP6 total cumulative applied water, and all pixels were less than 4% different. All but 4 pixels were less than 2% different between the applied water from the two products. The highest percentage differences were found at the boundaries of the Daymet dataset and likely reflect edge-effects that occurred during upscaling. Overall, we interpret this to mean that the historic bias-correction performed by the NASA NEX-GDDP-CMIP6 team using the GMFD dataset is adequate and similar enough to Daymet historical data that we can reasonably compare the two outputs and use them in series.

3.2.3 Potential Evapotranspiration: Theoretical Basis and Model Implementation

In this paper, we present PET calculated using the Penman (1948) approach. Broadly, when calculating PET, the choice of PET equation is driven by data availability and the conditions of the location being modeled (Tegos et al., 2015). Certain equations, such as Hargreaves-Samani, are designed to use minimal input data and often only rely on monthly temperature and precipitation (Cob and Tejero-Juste, 2004). However, these temperature-based equations miss the evaporation that can be driven by high solar radiation even in cold temperature, and radiation-based approaches are preferred. Within radiation-based approaches, certain equations, like the Penman-Monteith Equation or Shuttleworth and Wallace, require detailed parametrization of the vegetation and its interactions with the atmosphere or major assumptions based on a predetermined crop height (Allen et al., 1998). These equations tend to be considered as the standard to which other more simple or empirical calculations are compared (Xu and Singh, 2002). Other equations, such as the Priestley-Taylor Equation, do not perform well in arid regions (Ajjur and Al-Ghamdi, 2021).

Given the geospatial nature of this project and the need for an accurate equation that captured regional dynamics, we reviewed published methodologies for a radiation-based approach suitable for arid and non-arid regions primarily forced by physical factors. Selecting an equation that does not explicitly parameterize vegetation allows us to make minimal assumptions about the character and uniformity of vegetation or how the distribution of vegetation will change with climate change. The Penman (1948) equation, equation 19, is a physically based, PET approach that has been shown to perform well in arid environments (Li et al., 2016; Ajjur and Al-Ghamdi, 2021). Since the data requirements were also feasible, we determined the Penman (1948) equation to be well suited to modeling across the Western US.

$$PET = \frac{\Delta}{\Delta+\gamma}\left(\frac{R_n}{\lambda}\right) + \frac{\gamma}{\Delta+\gamma}E_a \tag{19}$$

In the Penman (1948) equation, PET (mm d^{-1}) of a saturated surface is a function of the slope of the vapor pressure curve (Δ; kPa $^{o}C^{-1}$), psychrometric constant (γ; kPa $^{o}C^{-1}$), net radiation (R_n; MJ m^{-2} d^{-1}), latent heat of vaporization (λ; MJ kg^{-1}), and E_a, a function of wind speed, vapor pressure, and saturation vapor pressure (mm d^{-1}). The methods presented here for calculating Penman PET are primarily drawn from McMahon et al. (2013) which presents a detailed supplement to support calculations. Equations are from McMahon et al. unless otherwise cited (2013). Other major sources for this methodology include Allen et al., (1998), Taheri et al., (2022), and Bjarke et al. (2023). PET, along with applied water, is calculated using daily meteorological inputs. The PET model written for this geospatial implementation includes four modules: vapor pressure, wind, psychrometric constant, and net radiation (Figure 7).

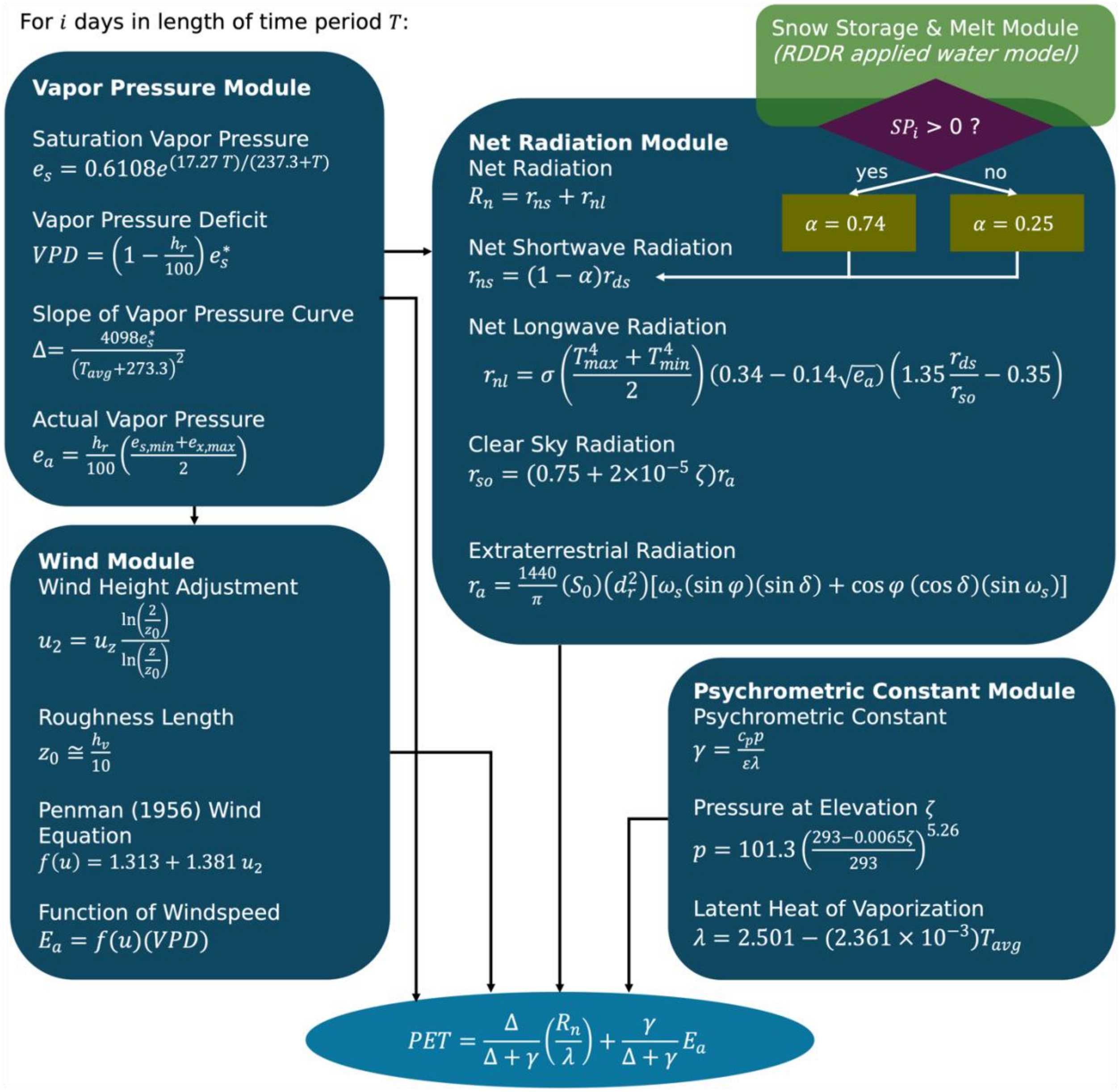

Figure 7: Overview of the Penman potential evapotranspiration (PET) model implementation. Four modules, the vapor pressure module, wind module, net radiation module, and psychrometric constant model, were used to calculate the final PET equation. The daily applied water model is fully integrated so that the presence or absence of snowpack on a given day can be used to select albedo.

The vapor pressure module includes saturation vapor pressure, vapor pressure deficit, and the slope of the vapor pressure curve. Saturation vapor pressure, e_s, is calculated using equation 20 (Bjarke et al., 2023):

$$e_s = 0.6108e^{(17.27\,T)/(237.3+T)} \tag{20}$$

where T is air temperature in ºC and e_s is in units of kPa. Daily saturation vapor pressure (e_s^*) is calculated from averaging the saturation vapor pressure for where T is set to each minimum daily temperature T_{min} and maximum daily temperature T_{max}, which correspond to $tasmin$ and $tasmax$ converted from K to ºC. Daily vapor pressure deficit (VPD) is calculated using equation 21 (Bjarke et al., 2023),

$$VPD = \left(1 - \frac{h_r}{100}\right) e_s^* \tag{21}$$

where e_s^* is daily saturation vapor pressure (kPa) and h_r is daily relative humidity (%), which is provided in CMIP6 data as $hurs$. Finally, the slope of the vapor pressure curve, Δ, is calculated using the following equation 22 (Bjarke et al., 2023):

$$\Delta = \frac{4098e_s^*}{\left(T_{avg}+273.3\right)^2} \tag{22}$$

where Δ is in units of kPa $ºC^{-1}$, e_s^* is daily saturation vapor pressure as calculated above (kPa) and T_{avg} is daily average temperature (ºC) for which we CMIP6 tas, converted to ºC.

The wind module depends on the results of the vapor pressure module and incorporates vegetation parameterization. Daily mean surface wind is modeled in the CMIP6 data at a height 10 m above the ground surface ($sfcWind$, m s^{-1}). We adjust wind height to 2 m to match the requisite input for Penman PET using equation 23,

$$u_2 = u_z \frac{\ln\left(\frac{2}{z_0}\right)}{\ln\left(\frac{z}{z_0}\right)} \tag{23}$$

where u_2 is wind speed 2 m above the surface (m s^{-1}), u_z is wind speed (m s^{-1}) at height z above the surface (m), and z_0 is roughness length (m). Roughness length is a function of vegetation height and can be approximated as 1/10th of the vegetation height (h_v):

$$z_0 \cong \frac{h_v}{10} \tag{24}$$

Given that preliminary analysis and potential sites for burial indicated that sagebrush or other woody vegetation would likely be the ground cover, we selected a vegetation height of 1 m for this analysis. Wind speed 2 m above the surface (u_2) is used in the wind equation used to calculate E_a (mm d^{-1}),

$$E_a = f(u)(VPD) \tag{25}$$

where $f(u)$ is a wind equation and VPD is vapor pressure deficit (kPa). Several wind equations exist to relate the effect of wind to PET, and we chose Penman's 1956 wind equation based on previous studies finding that earlier wind equations were inaccurate (Linacre, 1993; Cohen et al., 2002). The Penman (1956) wind equation is defined in equation 26.

$$f(u) = 1.313 + 1.381u_2 \tag{26}$$

The next module is the psychrometric constant module. The psychrometric constant (γ; kPa ºC^{-1}) is calculated using formula 27 (Allen et al., 1998),

$$\gamma = \frac{c_p p}{\varepsilon\lambda} \tag{27}$$

where c_p is the specific heat of water at constant pressure (1.013 x 10^{-3} MJ kg^{-1} ºC^{-1}), p is atmospheric pressure at the ground surface, ε is the ratio of the molecular weight of water vapor to dry air (0.622), and λ is the latent heat of vaporization. Atmospheric pressure, p, is a function of elevation and is calculated using the elevation netCDF already discussed using the following formula in equation 28 (Allen et al., 1998):

$$p = 101.3\left(\frac{293-0.0065\zeta}{293}\right)^{5.26} \tag{28}$$

In this equation, ζ is elevation above sea level in meters. Latent heat of vaporization (λ; MJ kg^{-1}) was calculated on a daily using daily average temperature (T_{avg}; °C) for a given pixel using the following equation 29.

$$\lambda = 2.501 - (2.361 \times 10^{-3})T_{avg} \tag{29}$$

The most involved module is the net radiation module. Most GCMs include output for incoming and outgoing shortwave and longwave radiation as well as sensible and latent heat fluxes from surface processes and geothermal heat. These variables allow for net radiation to be calculated simply (Bjarke et al., 2023). However, the downscaled CMIP6 data used does not included the full set of radiation parameters and only includes surface downwelling shortwave radiation ($rsds$) and surface downwelling longwave radiation ($rlds$). Since geothermal radiation and heat fluxes from surface processes are many orders of magnitude smaller than solar radiation, they can be effectively ignored in the surface heat flux (Davies and Davies, 2010; Kopp & Lean, 2011). As such, we calculate net radiation using equation 30:

$$R_n = r_{ns} + r_{nl} \tag{30}$$

where r_{ns} is net surface shortwave radiation and r_{nl} is net surface longwave radiation.
Net surface shortwave radiation can be determined with surface downwelling shortwave radiation and ground surface albedo. We used a surface albedo of 0.25 which is representative of semi-desert (Douglas et al., 2009). We integrated the applied water module into the PET model, and as such, we used a surface albedo of 0.74 as discussed in section 2.2.4 when snow was modeled to be present. Net surface shortwave radiation was calculated using equation 31.

$$r_{ns} = (1-\alpha)r_{ds} \tag{31}$$

In this equation, r_{ns} is net surface shortwave radiation (MJ m^{-2} d^{-1}), r_{ds} is downwelling surface shortwave radiation (MJ m^{-2} d^{-1}), and albedo, as described above, is dimensionless. Note that downwelling surface shortwave radiation must be converted from units of W m^2 in $rsds$ to units of MJ m^{-2} d^{-1}.

Net surface longwave radiation can be calculated as a function that accounts for vapor pressure, air temperature, and cloud cover. The overall formula for net surface longwave radiation is described in equation 32,

$$r_{nl} = \sigma\left(\frac{T_{max}^4 + T_{min}^4}{2}\right)\left(0.34 - 0.14\sqrt{e_a}\right)\left(1.35\frac{r_{ds}}{r_{so}} - 0.35\right) \tag{32}$$

where σ is Stefan-Boltzmann's constant (5.67 x 10^{-8} W m^{-2} K^{-4}), T_{max} and T_{min} are maximum and minimum daily air temperature respectively, e_a is actual vapor pressure (kPa), r_{ds} is downwelling surface shortwave radiation (MJ m^{-2} d^{-1}), and r_{so} is clear sky radiation (MJ m^{-2} d^{-1}) (Cleugh et al, 2005; Taheri et al., 2022). Actual vapor pressure (e_a) is approximated from relative humidity (h_r; %) and the average saturation vapor pressure between T_{min} ($e_{s,min}$) and T_{max} ($e_{s,max}$) in equation 33 (Taheri et al., 2022).

$$e_a = \frac{h_r}{100}\left(\frac{e_{s,min} + e_{x,max}}{2}\right) \tag{33}$$

Cloud cover is approximated by the ratio between downwelling surface shortwave radiation and clear sky radiation. Clear sky radiation is a function of elevation and extraterrestrial radiation as shown in equation 34, where ζ is elevation above sea level (m) and r_a is extraterrestrial radiation (MJ m^{-2} d^{-1}).

$$r_{so} = (0.75 + 2 \times 10^{-5}\ \zeta)r_a \tag{34}$$

Extraterrestrial radiation is calculated from solar declination and the sunset angle, which are function so of the day of year and pixel latitude (Equation 35).

$$r_a = \frac{1440}{\pi}(S_0)(d_r^2)[\omega_s(\sin\varphi)(\sin\delta) + \cos\varphi\,(\cos\delta)(\sin\omega_s)] \tag{35}$$

In this equation, S_0 is the solar constant (0.0820 MJ m^{-2} min^{-1}; by convention, multiplied by 1440 in the first term of r_a to convert to units of MJ m^{-2} min^{-1}), d_r is the inverse relative Earth-Sun distance (dimensionless), ω_s is the sunset hour angle (rad), φ is latitude (rad), and δ is solar declination (rad). The latitude of the centroid of each CMIP6 pixel was converted to radians and used for latitude (φ). The square of the inverse relative Earth-Sun distance is a function of the day of year (DoY) (Equation 36).

$$d_r^2 = 1 + 0.033\cos\left(\frac{2\pi}{365}\,DoY\right) \tag{36}$$

Solar declination (δ) is also a function of DoY (Equation 37).

$$\delta = 0.409\sin\left(\frac{2\pi}{365}DoY - 1.39\right) \tag{37}$$

Sunset hour angle (ω_s) is calculated with equation 38.

$$\omega_s = \arccos[-\tan(\varphi)\tan(\delta)] \tag{38}$$

3.2.4 Aridity Index

We calculated aridity index (AI) for all the cumulative time steps (monthly, seasonally, annually) by dividing cumulative precipitation by cumulative PET for each time step (Equation 39), following the convention set by UNEP (1992).

$$AI = \frac{P}{PET} \tag{39}$$

The resulting non-dimensional number was analyzed both numerically and using the classification scheme provided by UNEP (1992) and provided in table 4.

Classification	Aridity Index Threshold
Hyperarid	AI < 0.05
Arid	0.05 ≤ AI < 0.20
Semi-arid	0.20 ≤ AI < 0.50
Dry Subhumid	0.50 ≤ AI < 0.65

Table 4: Aridity index classifications from UNEP (1992).

3.2.5 Analysis of CMIP6 Products

All CMIP6 GCM ensemble products were aggregated into annual, seasonal, and monthly time steps. Precipitation, applied water, and PET were aggregated by summing daily data for the duration of each time step. Aridity index was calculated from the precipitation and PET products already summed to that timestep. Seasonal partitions were created following meteorological convention for the Northern Hemisphere: winter is December, January, and February (DJF), spring is March, April, and May (MAM), summer is June, July, and August (JJA), and fall is September, October, and November (SON). All timesteps (annual, seasonal, and monthly) were averaged into 20-year periods to describe conditions from 1991 to 2100. The historical time period was defined as 1991-2010. Four future time periods were calculated to each SSP: near-future (2021-2040), mid-century (2041-2060), late-century (2061-2080), and end-century (2081-2100). These time averages were performed on the ensemble data. For the historical period, 1990 was used as an initialization year for the applied water model and removed before temporal averaging. For the future time period ranging from 2021 to 2100 for each SSP, 2020 was used as the initialization year and removed. The change between each consecutive future time period was calculated, as well as the difference between each time period and the historical time period.

The primary product used to understand the projected change in conditions relevant for biomass burial was the difference between the maximum seasonal aridity index from all years and all seasons from 2021-2100 for each SSP compared to the maximum historical aridity index

(1991-2010) for a given pixel. Since water balance cannot be calculated without AET, aridity index captures the next most relevant information about the magnitudes of precipitation and evapotranspiration relative to each other. The seasonal timestep was used because it captures the interannual variability and seasonality of precipitation and evapotranspiration on a time scale that is simultaneously broad enough to not overstate the precision of the data due to uncertainties of climate modeling.

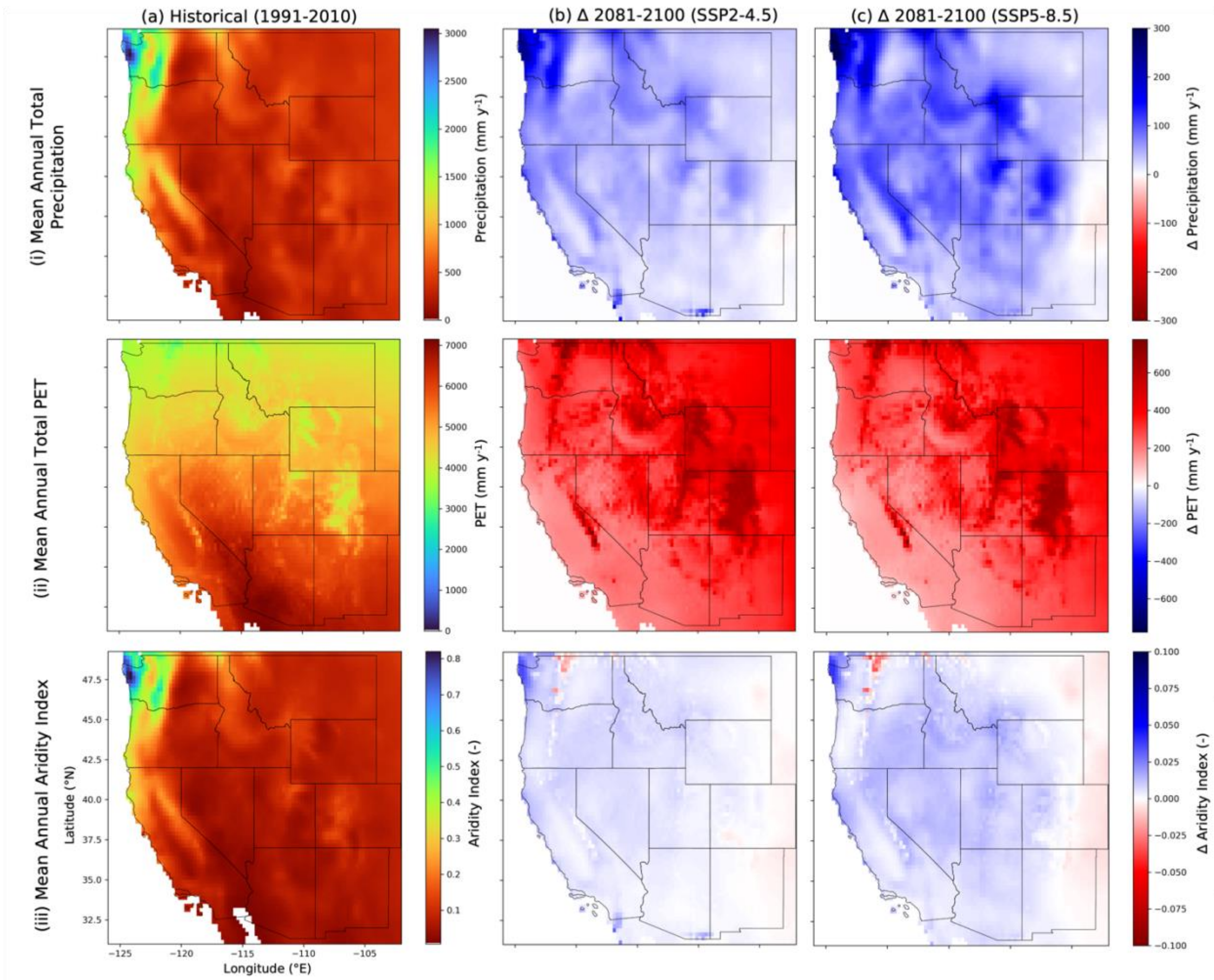

Figure 8: Average annual total precipitation (row i), total PET (row ii), and aridity index (row iii) for the historical, 1991-2010, time period (column a), and the change between the historical time period and the end century projection, 2081-2100, time period under SSP2-4.5 (column b) and SSP5-8.5 (column c) for each variable.

3.3 Results

3.3.1 Interannual Results of Historical and Future Modeling

Mean annual total precipitation and PET are projected to predominantly increase under both SSPs from the historical period (1991-2010) to the end-century time period (2081-2100) (Figure 8). Increases in both total precipitation and PET are larger under SSP5-8.5 than SSP2-4.5. West of the Rocky Mountains, annual aridity index broadly increases (more humid) by 0.025 or less for SSP5-8.5 and 0.015 or less for SSP2-4.5. Annual aridity index is projected to decrease (more arid) in the Cascade Mountains by up to 0.08. East of the Rocky Mountains, annual aridity index is projected to slightly decrease (more arid) by less than 0.01.

On the interannual scale, total applied water and precipitation are identical. In the historical time period, minimum mean annual total precipitation is 43 mm in the Sonoran Desert, and the maximum is 3048 mm in the Coast Range of Washington. Precipitation increases from the historical to end-century time period by up to 250 mm under SSP2-4.5 and 316 mm under SSP5-8.5. These maximum increases occur in the Pacific Northwest where precipitation is already high (> 2500 mm) relative to the rest of the region of interest. Small decreases in precipitation are projected in the southeastern corner of Colorado and northeastern corner of New Mexico, with the largest decreases being 6 mm and 13 mm for SSP2-4.5 and SSP5-8.5, respectively. Increases in precipitation are greatest along mountain ranges and high topography, and these increases are relatively uniform, aside from the Cascades and the Pacific Northwest coastal ranges, despite differing historical precipitation amounts. Changes in precipitation are noticeably smaller (< 25 mm) on the leeward side (Eastern side) of the Cascade Range in Washington (Columbia Plateau), Wasatch Range in Utah, and Rocky Mountains in Wyoming and Colorado. Across all four time periods for each SSP, there are broadly the same geospatial patterns as described above but there are regions where the trend of precipitation change alters direction between time periods (Figures 9 and 10).

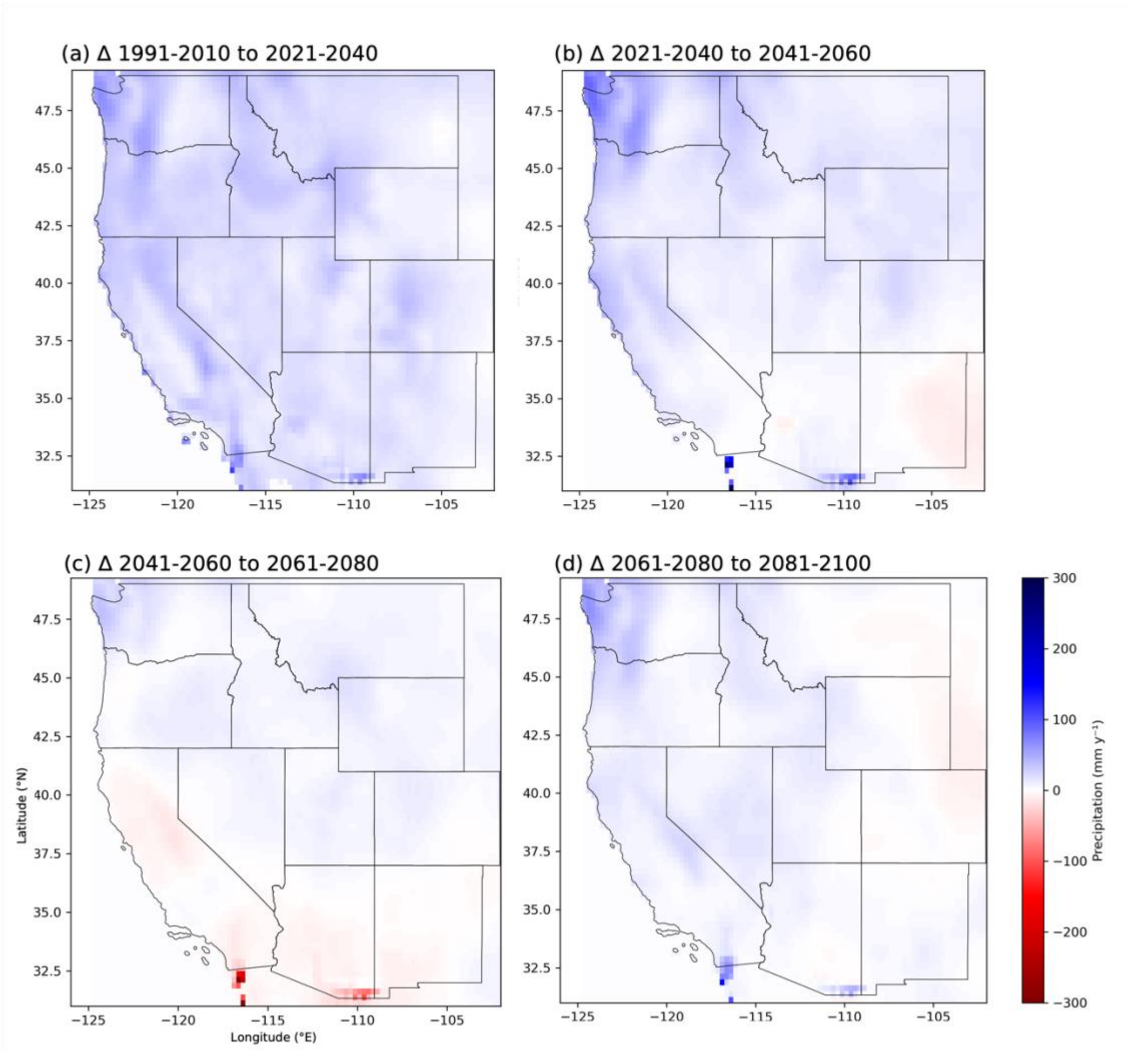

Figure 9: Change in mean annual total precipitation across all time periods for SSP2-4.5.

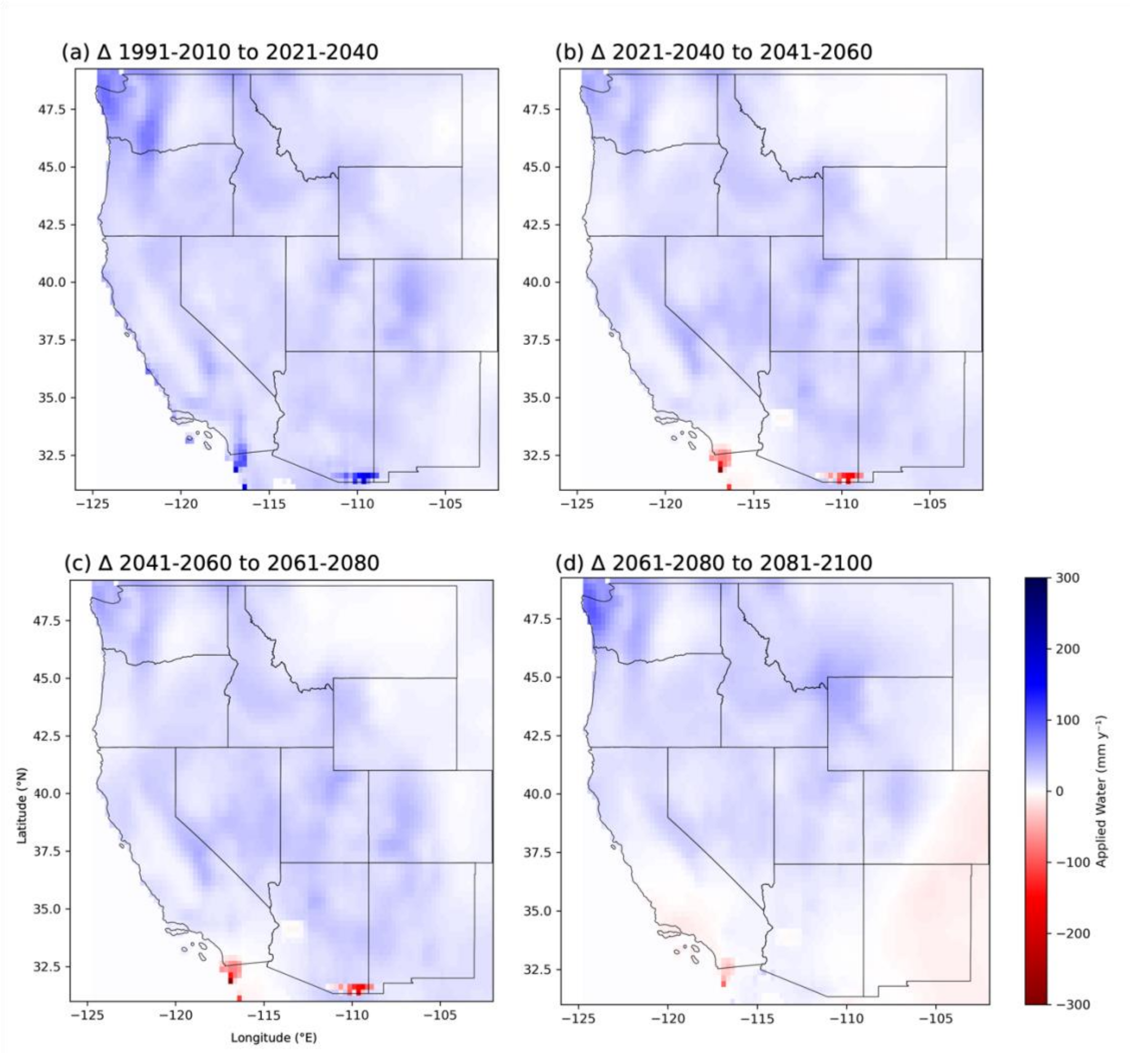

Figure 10: Change in mean annual total precipitation across all time periods for SSP5-8.5.

Projected increases in mean annual total PET are highest in areas with high topography (Figure 8). In the historical time period, mean annual total PET ranges from 2900 mm per year in the high Rocky Mountains and near the Canadian border to as high as nearly 6900 mm in the Sonoran Desert in southwestern Arizona and southeastern California. This trend broadly follows a latitudinal gradient where PET is inversely related to latitude. Mean annual total PET is projected to increase by up to 478 mm and 749 mm for SSP2-4.5 and SSP5-8.5, respectively, with highest increases in the Rocky Mountains, Cascade Range, and the Sierra Nevada Mountains. The smallest increases in PET occur along the coast of California with minimum

PET increases of 68 mm and 71 mm for SSP2-4.5 and SSP5-8.5, respectively. Outside of the changes resulting from topography, there is a gradient in the increase in PET from lower increases in the southwest along the California coast and greater increases moving northeast. Across all time periods for both SSPs, mean annual total PET consistently increases (Figures 11 and 12).

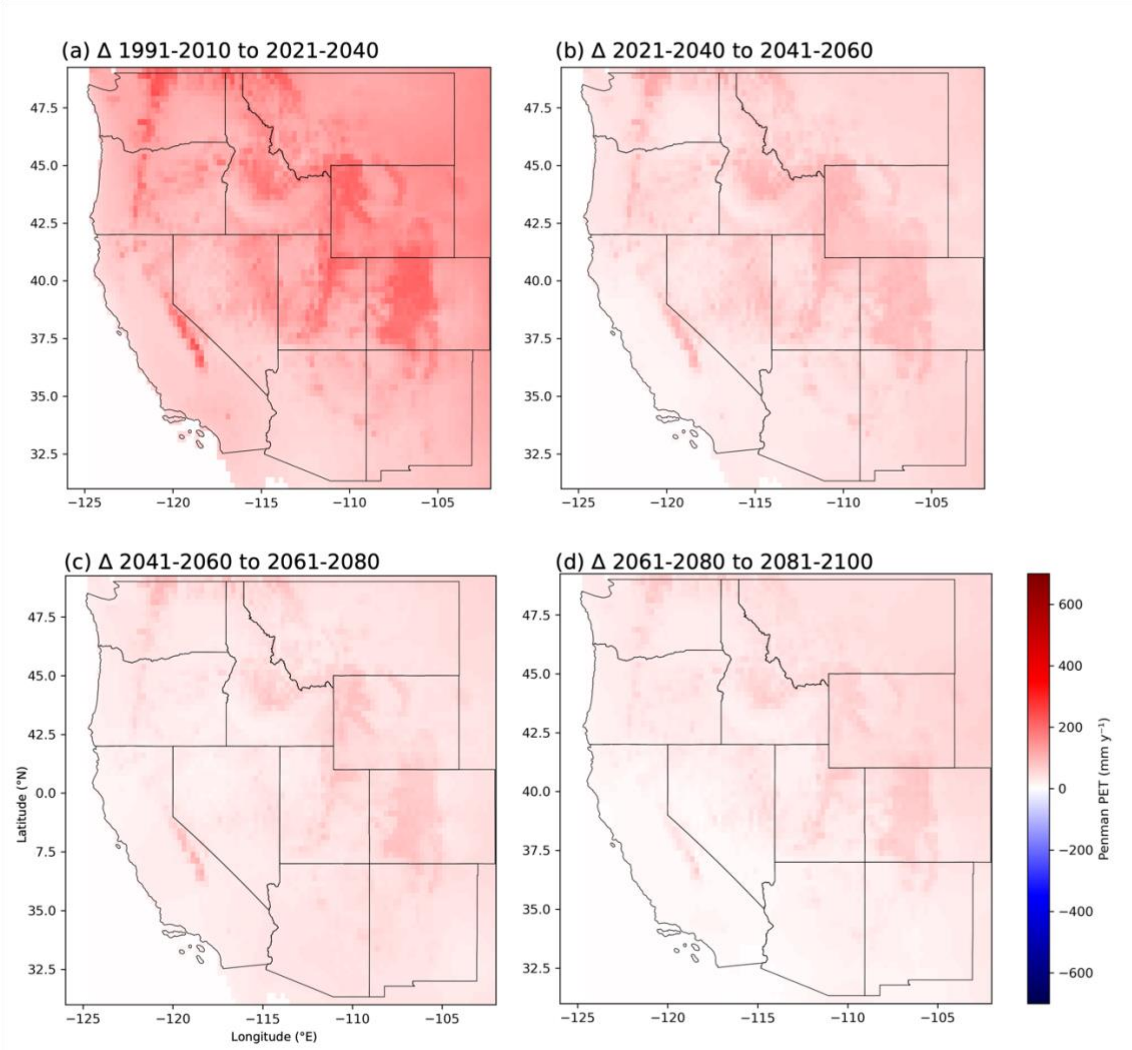

Figure 11: Change in mean annual total PET across all time periods for SSP2-4.5.

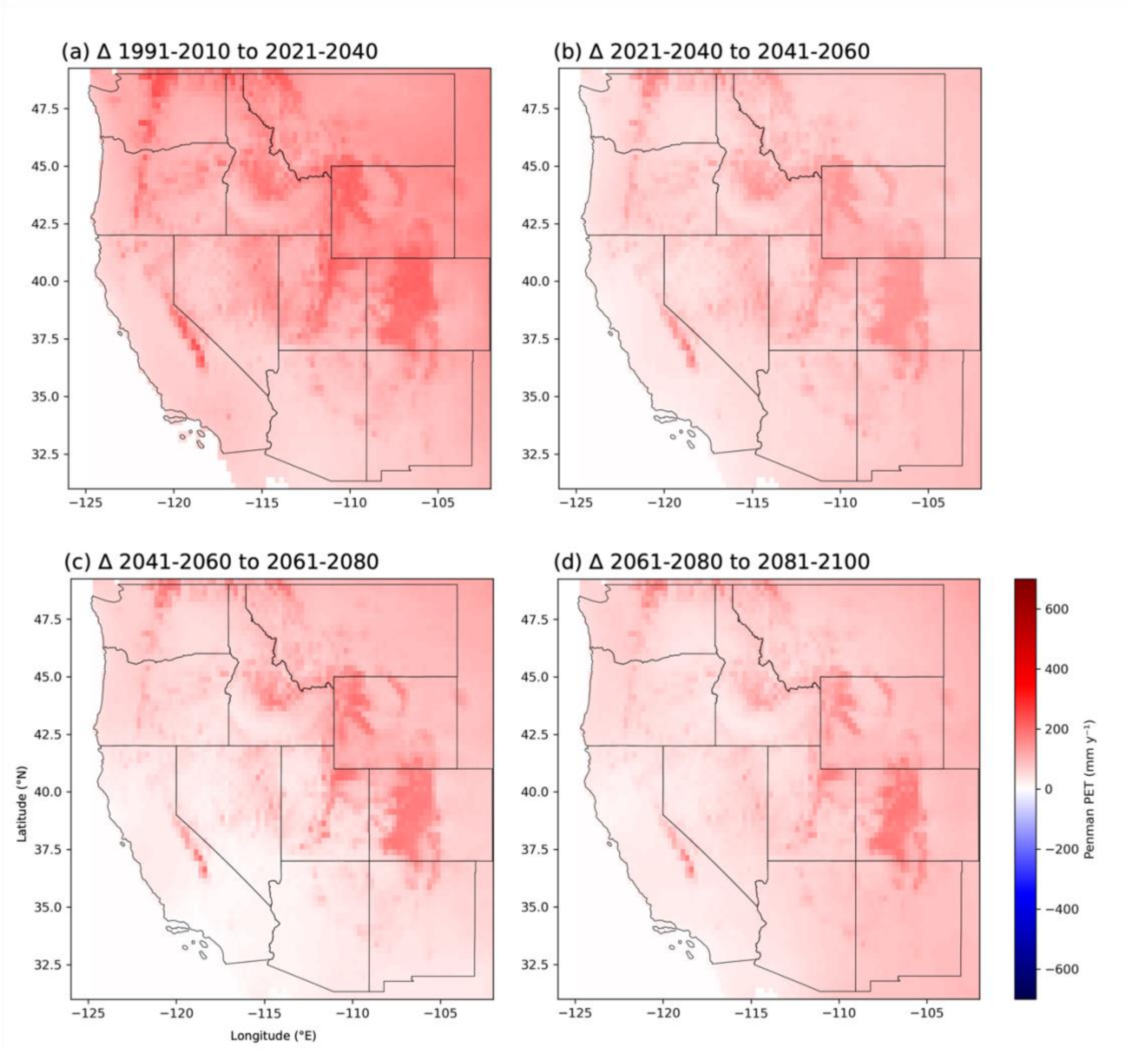

Figure 12: Change in mean annual total PET across all time periods for SSP5-8.5.

Mean annual aridity index is projected to increase in by the end-century time period in the majority of the Western US under both SSPs (Figure 8). The most arid region has its southern end in the Sonoran Desert in Arizona and California and stretches northward into Nevada along the leeward side of the Sierra Nevadas, and the aridity index for these pixels is less than 0.03. High topography is broadly less arid than regions with lower elevation, and low elevation regions on the leeward side of high topography are distinctly more arid. The highest aridity index values (most humid) are in the Cascade and Coast Ranges in Washington. To the west of the Rocky Mountains, aridity index is projected to slightly increase by the end-century time period under both SSPs. The significance of these changes is not well constrained in the current analysis. The largest changes in aridity index are projected in Washington with the Coast Range increasing by up to 0.1 and the pixels in the Cascades near the Canadian border decreasing by ~0.05 under SSP5-8.5, with smaller corresponding changes. Both of these regions occur where the highest aridity index values are observed in the historical time period. For some regions such as in California and Washington, the predicted trend in aridity index reverses direction throughout the 21st century (Figures 13 and 14). The trend reversal is more evident in SSP2-4.5 than SSP5-8.5.

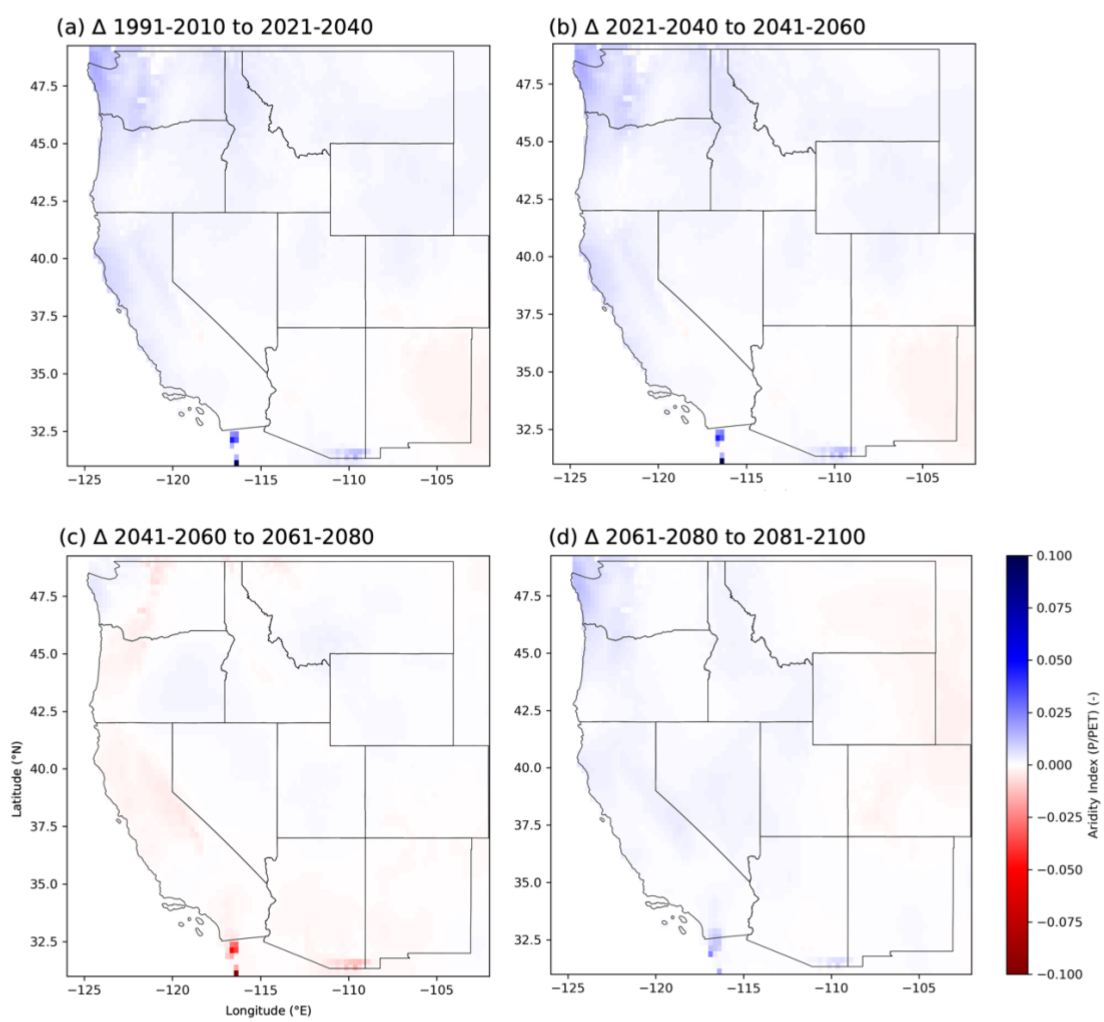

Figure 13: Change in mean annual aridity index across all time periods for SSP2-4.5.

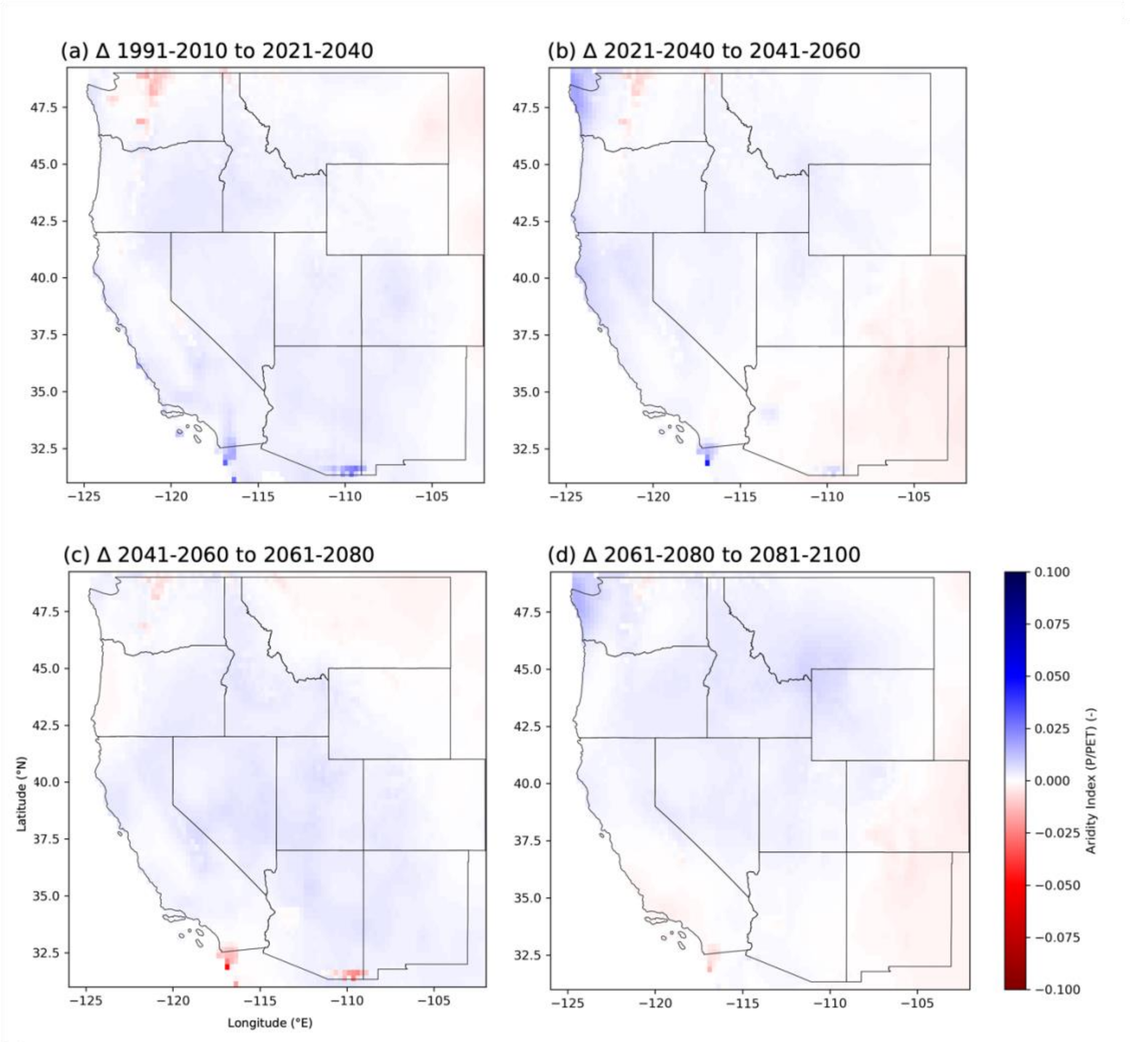

Figure 14: Change in mean annual aridity index across all time periods for SSP5-8.5.

3.3.2 Seasonal Changes from Historical to Future Climate Scenarios

Historical precipitation in the Western US is highly seasonally variable for most of the region (Figure 15a). Precipitation is consistently high across seasons in Coast Range and Cascades in Washington and consistently low in the Sonoran Desert and Columbia Plateau. The Great Plains east or the Rocky Mountains and Arizona and New Mexico historically have higher precipitation in the summer while the central coast and Central Valley of California on average receive no precipitation in June, July, and August. As observed in the mean annual total precipitation trends in Figures 8-10, precipitation is predominantly projected to increase with the greatest increases occurring in the Pacific Northwest. Spring precipitation in the southern portion of the Western US is projected to decrease and, in the northern portion, it's projected to increase. The magnitude of change under SSP5-8.5 is larger than SSP2-4.5. Summer precipitation is projected to increase in an elliptical region covering California, Nevada, most of Oregon, southern Idaho, southwestern Wyoming, western Colorado, New Mexico, Utah, and Arizona. Outside of this elliptical region, summer precipitation is projected to decrease. Again, the magnitudes of the changes are higher under SSP5-8.5 than SSP2-4.5. Winter precipitation is projected to increase, predominantly with larger increases corresponding to higher topography such as the Sierra Nevadas and Rocky Mountains.

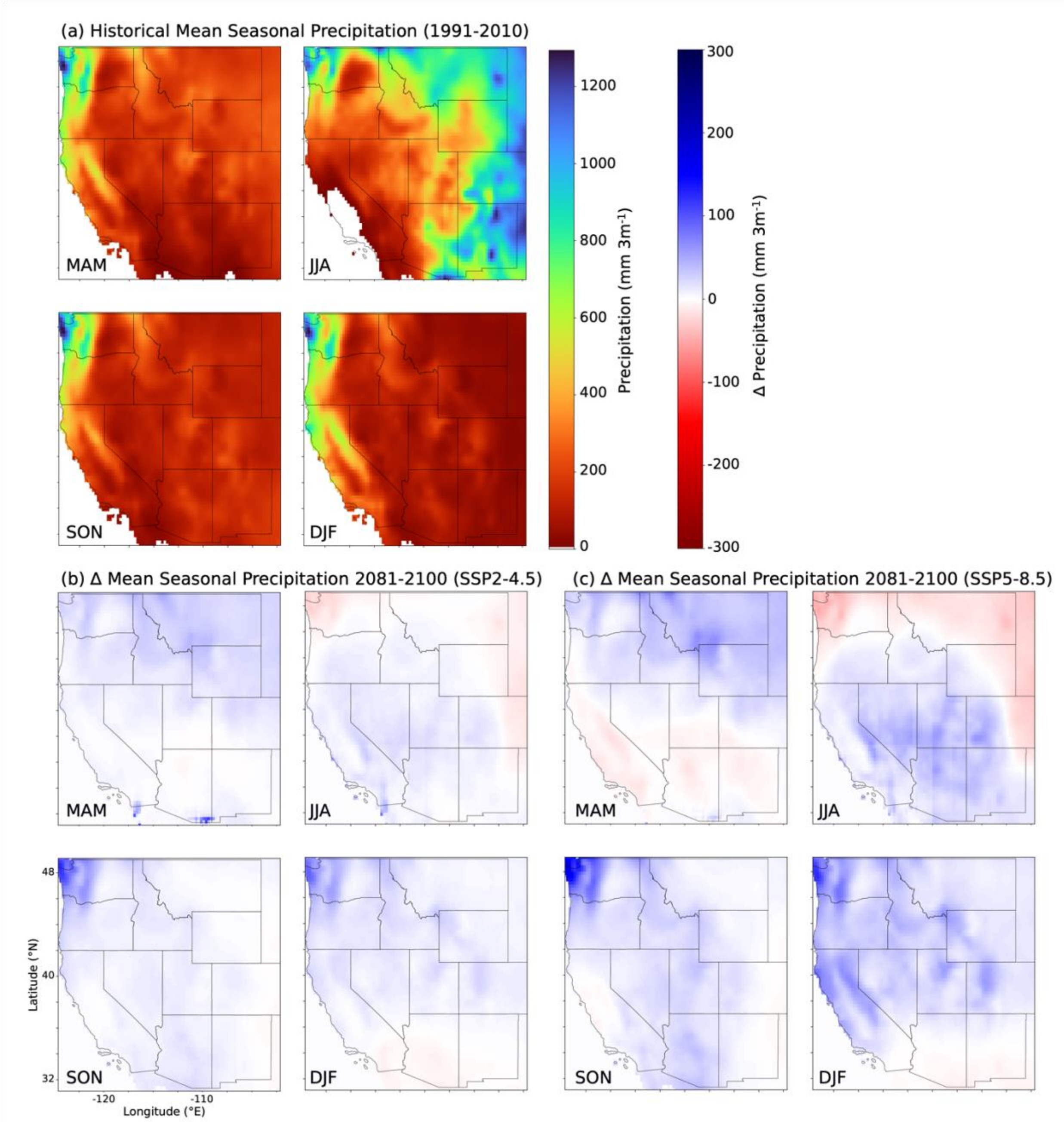

Figure 15: Seasonal historical (1991-2010) mean total precipitation (a) and the projected change from historical to end-century (2081-2100) seasonal precipitation under SSP2-4.5 (b) and SSP5-8.5 (c). "MAM" represents months March, April, and May (spring), "JJA" represents months June, July, and August (summer), "SON" represents months September, October, and November (fall), and "DJF" represents months December, January, and February (Winter).

Seasonal applied water is distinct from seasonal precipitation due to the accumulation and melting of snowpack. The seasonal distribution of historic applied water and projected changes have the same general trends and geospatial distribution as seasonal precipitation with the notable exception of high elevation regions in the Sierra Nevadas, Rocky Mountains, and Cascade Range in the fall, winter, and spring seasons (Figure 16). In high elevation regions, winter applied water is lower than precipitation and spring applied water is higher than precipitation due to the presence of snowpack. For SSP5-8.5, the change in applied water from the historical to end-century time period shows a decrease in spring applied water of approximately 50 to 200 mm and an increase in winter applied water of similar magnitude. The same trend is observed under SSP2-4.5, but the magnitude of change is smaller. Summer historical applied water and end-century change in applied water are nearly identical to the precipitation equivalents since the influence of snowpack in the summer is very small and affects few pixels.

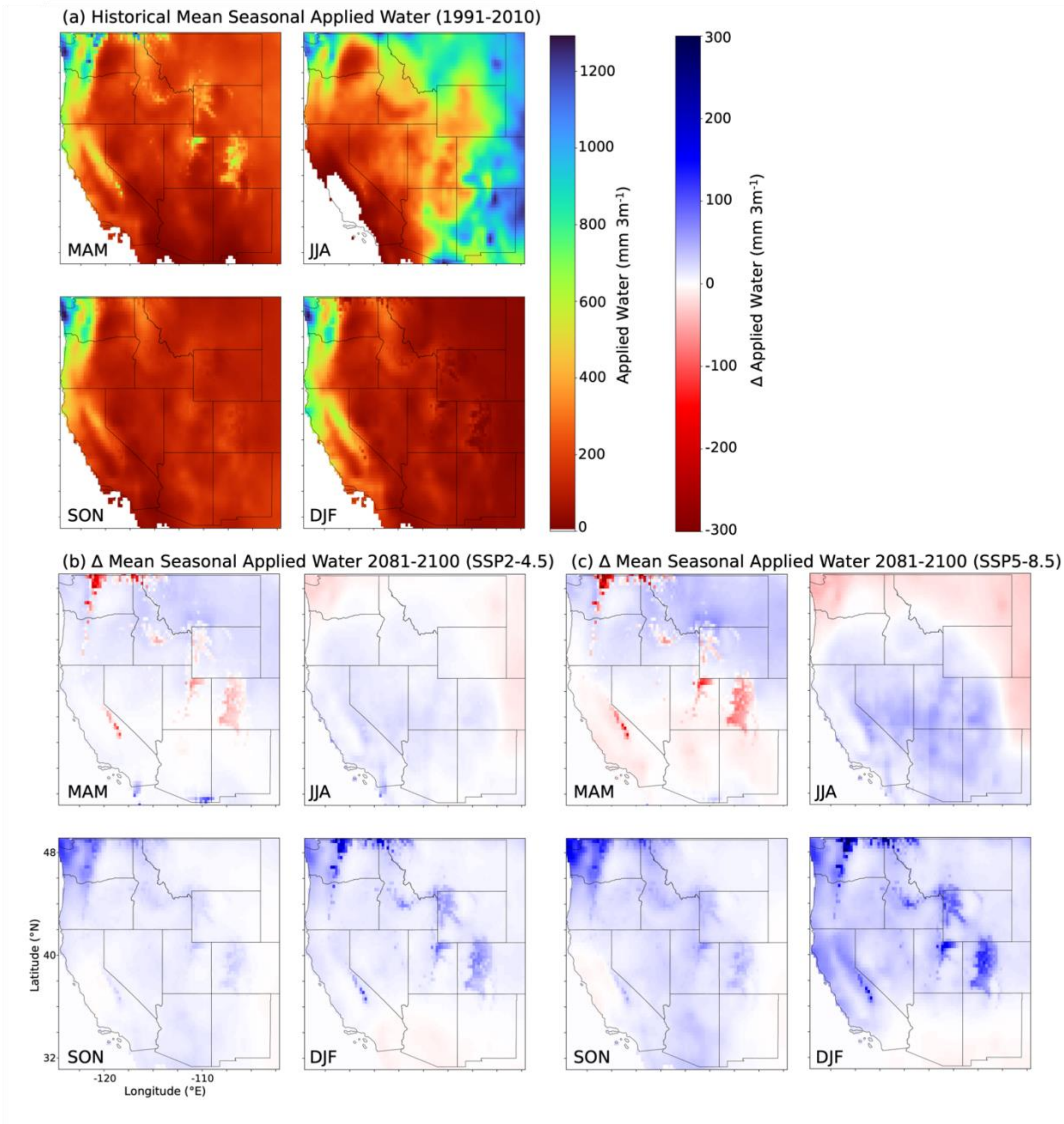

Figure 16: Seasonal historical (1991-2010) mean total applied water (a) and the projected change from historical to end-century (2081-2100) seasonal applied water under SSP2-4.5 (b) and SSP5-8.5 (c). "MAM" represents months March, April, and May (spring), "JJA" represents months June, July, and August (summer), "SON" represents months September, October, and November (fall), and "DJF" represents months December, January, and February (Winter).

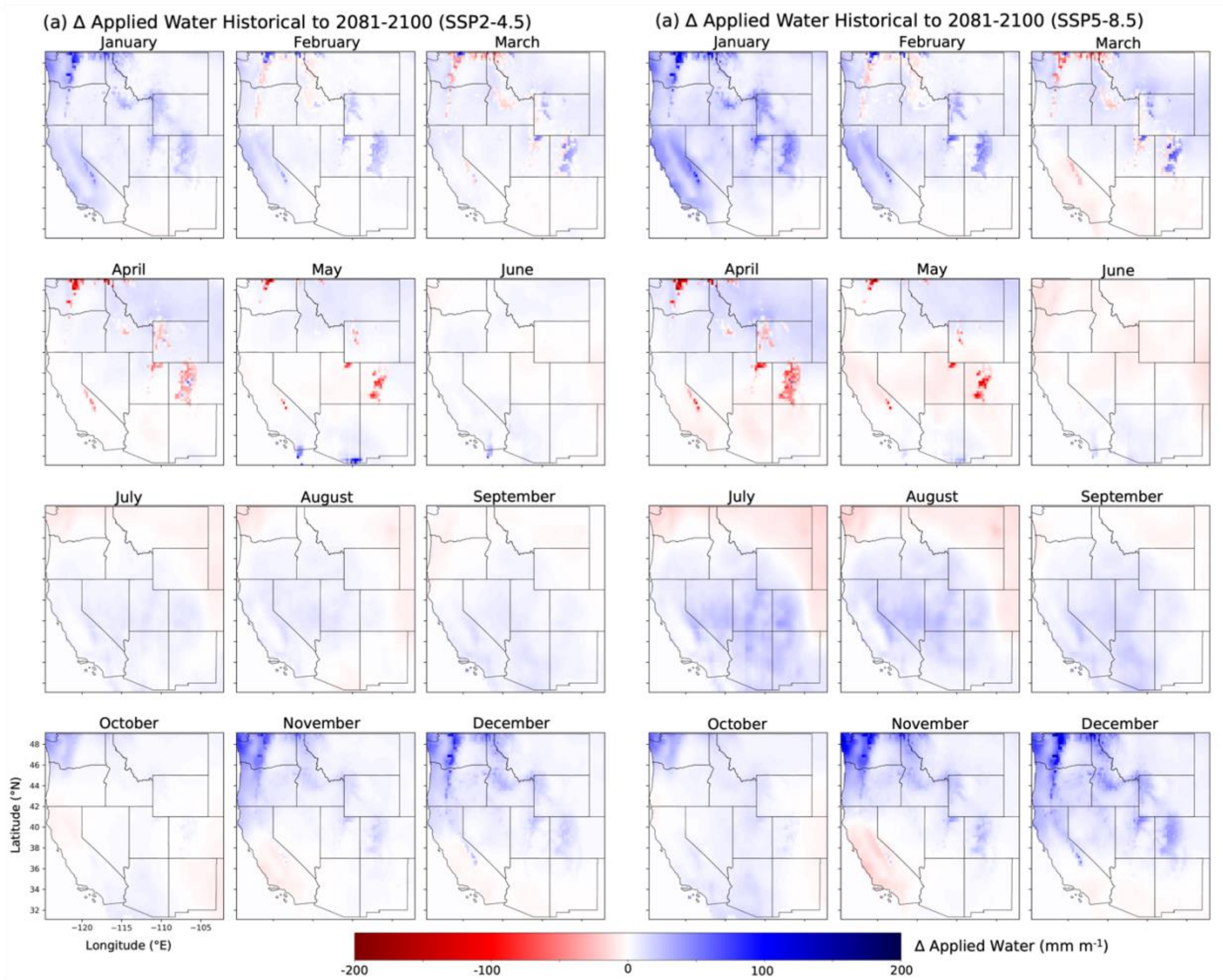

Figure 17: Monthly change in applied water for the end-century time period (2081-2100) from the historical time period (1991-2010) under (a) SSP2-4.5 and (b) SSP5-8.5.

Seasonal PET reflects the latitudinal gradient observable in annual data (Figures 8, 18). PET is highest in the summer for most regions except for the subtropical deserts at the southern borders of California, Arizona, and New Mexico. PET is lowest in the winter. Spring and fall PET have similar trends and distributions, but, in the historic simulation, PET at high elevations is lower in the spring than the fall. The end-century change in PET is notably highest in these high elevation regions in fall, winter, and spring, and the spring changes are the largest with projected changes in seasonal total PET up to 450 mm. As seen in the annual total PET (Figure

8), seasonal total PET is projected to increase with the exception of parts of California, Nevada, and Arizona in the summer under SSP5-8.5.

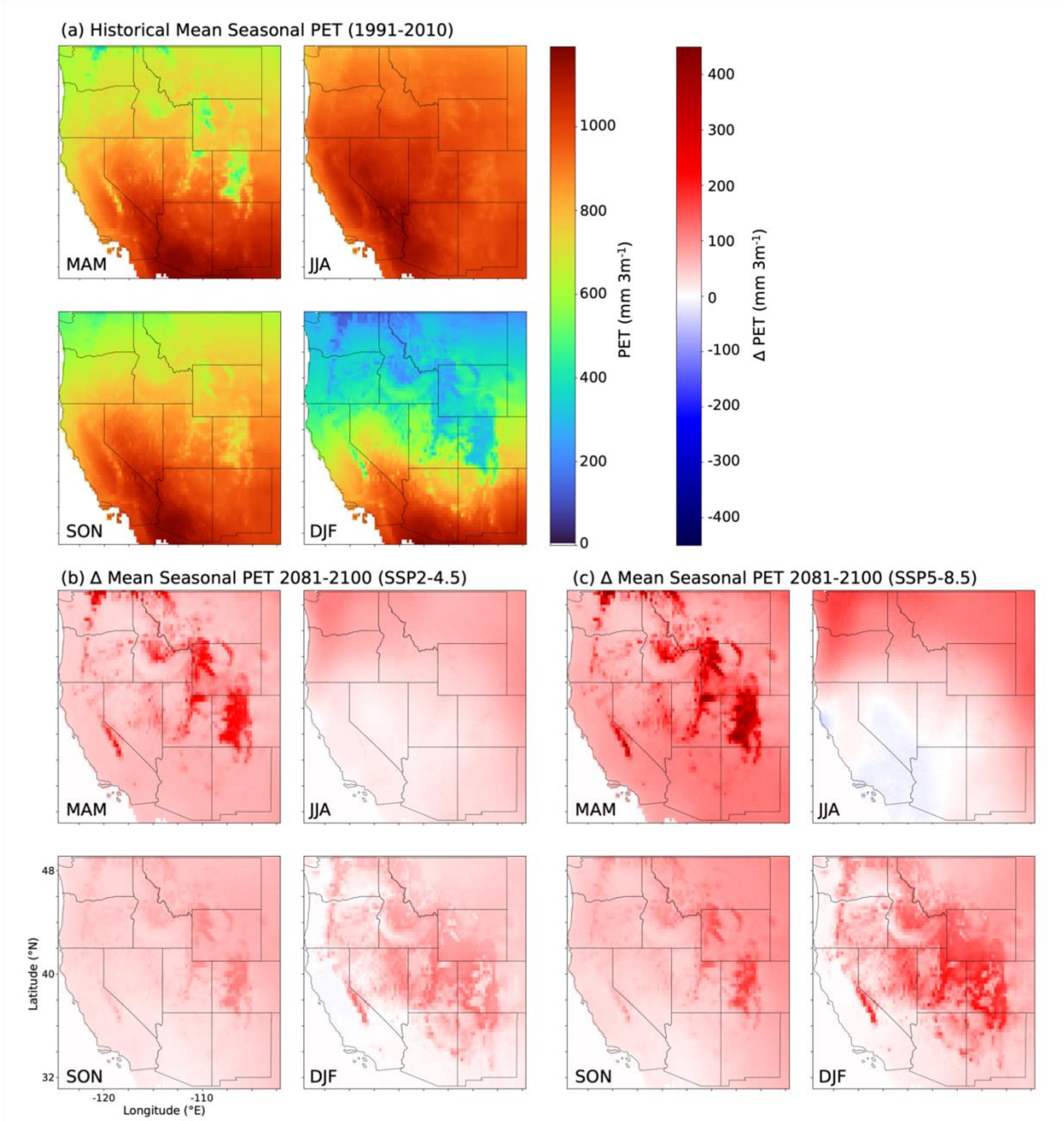

Figure 18: Seasonal historical (1991-2010) mean total PET (a) and the projected change from historical to end-century (2081-2100) seasonal PET under SSP2-4.5 (b) and SSP5-8.5 (c). "MAM" represents months March, April, and May (spring), "JJA" represents months June, July, and August (summer), "SON" represents months September, October, and November (fall), and "DJF" represents months December, January, and February (Winter).

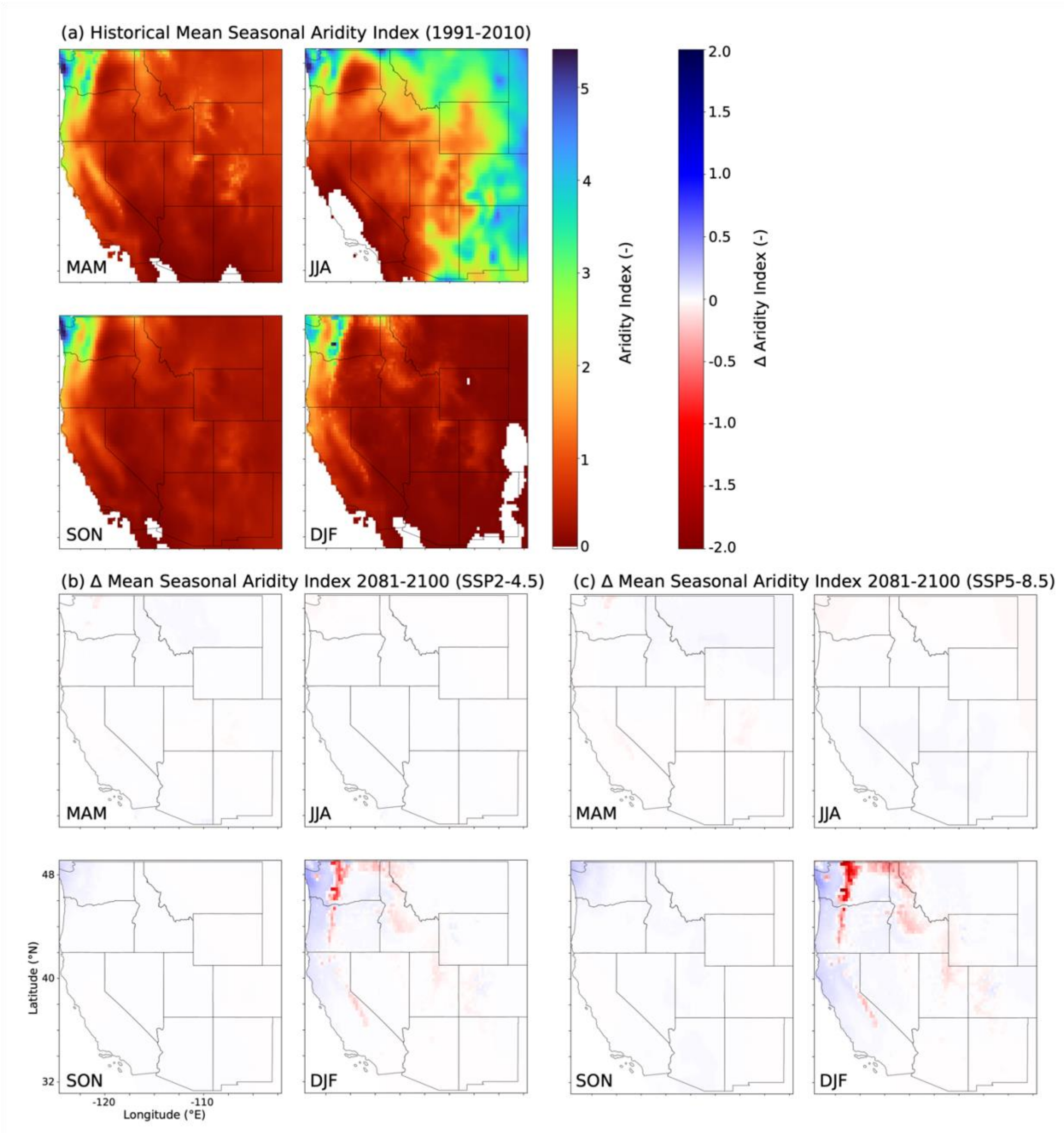

Figure 19: Seasonal historical (1991-2010) mean aridity index (a) and the projected change from historical to end-century (2081-2100) seasonal aridity index under SSP2-4.5 (b) and SSP5-8.5 (c). "MAM" represents months March, April, and May (spring), "JJA" represents months June, July, and August (summer), "SON" represents months September, October, and November (fall), and "DJF" represents months December, January, and February (Winter).

Aridity index, due to the formulation of the index, follows a distribution like that of precipitation and PET (Figures 15, 18, 19). The projected change in seasonal aridity index from the historical time period to end-century is minimal in spring, summer, and fall with the exception of a small increase in aridity index in Washington in the fall season under both SSPs (Figure 19). The largest trend is observable in the winter season, with decreases (becoming more arid) in aridity index up to 2 and increases up to 0.5 (becoming more humid). Winter seasonal aridity index is projected to increase at similar magnitudes along the Pacific Coast. The Cascade Range and the Northern Rockies have the largest projected decrease in aridity index. These results are reflected in the monthly time step data, with the largest changes occurring from November through March (Figure 20).

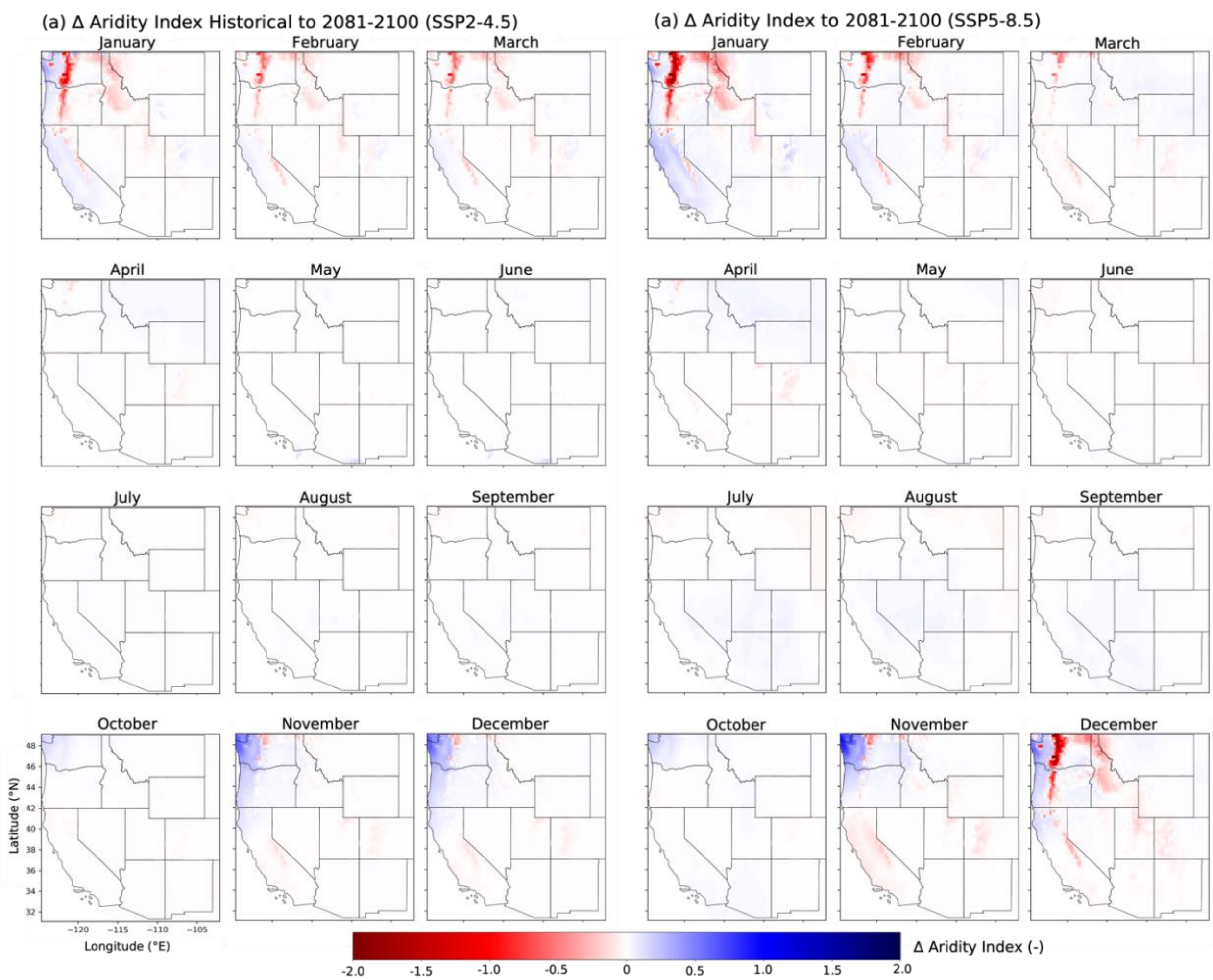

Figure 20: Monthly change in aridity index for the end-century time period (2081-2100) from the historical time period (1991-2010) under (a) SSP2-4.5 and (b) SSP5-8.5.

3.3.3 Implications of Climate Modeling for Minimum Required Cover Thickness

On a mean annual basis, the change between aridity index classifications across the Western US in the historical and end-century time periods is low (Figure 21). Under both SSPs, there is a decrease in area classified as hyperarid in the end century time period, and this decrease is greater in SSP5-8.5 than SSP2-4.5. These decreases occur at the hyperarid/arid interface, and the most notable decreases occur in the Colorado Plateau near the four corners region and in Nevada. Regions classified as semi-arid and above (more humid) do not change in distribution. Most of the Western US by land area is classified as arid and is projected to remain under this classification in the end-century time period under both SSPs. Areas modeled to have potential for woody biomass burial with minimum cover thicknesses less than 5 m fall within the hyperarid and arid regions.

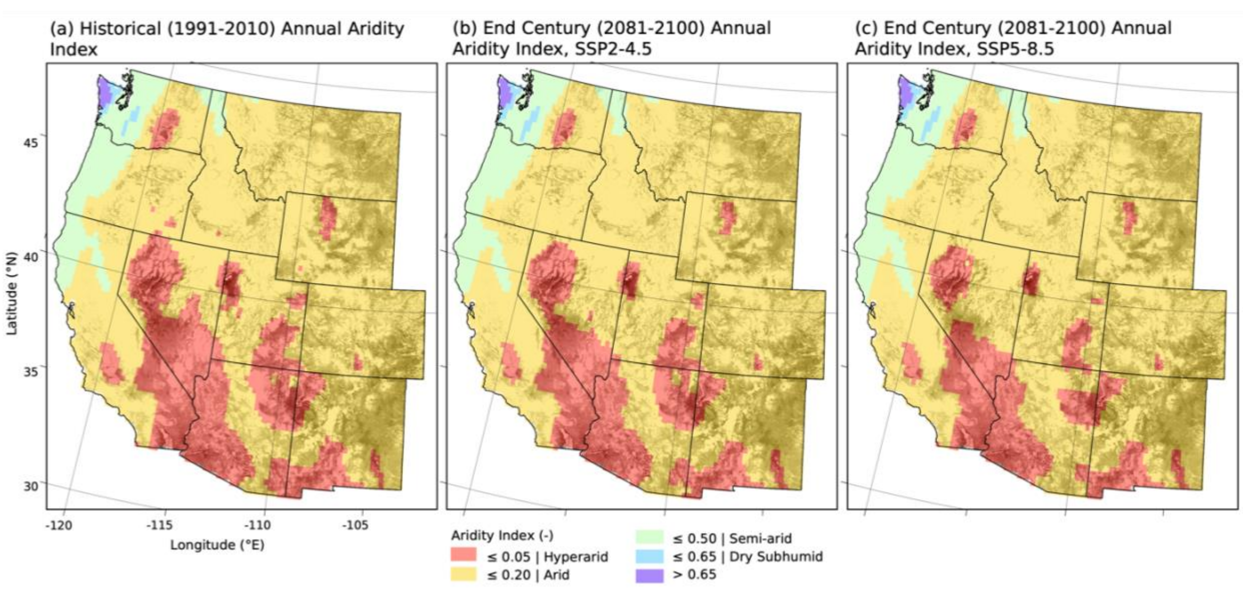

Figure 21: Aridity index classifications following UNEP (1992) standard for the (a) mean annual historical (1991-2010) aridity index, (b) projected mean annual end century (2081-2100) aridity index under SSP2-4.5, and (c) projected mean annual end century aridity index under SSP5-8.5. The colors are semi-transparent and overly a grayscale of the minimum required cover thickness derived from 95th percentile required water storage ($L_{V3,95}$) ranging from required thickness near 0 m (darkest) to 5 m (lightest). Areas with a minimum required cover thickness greater than 5 m are not displayed.

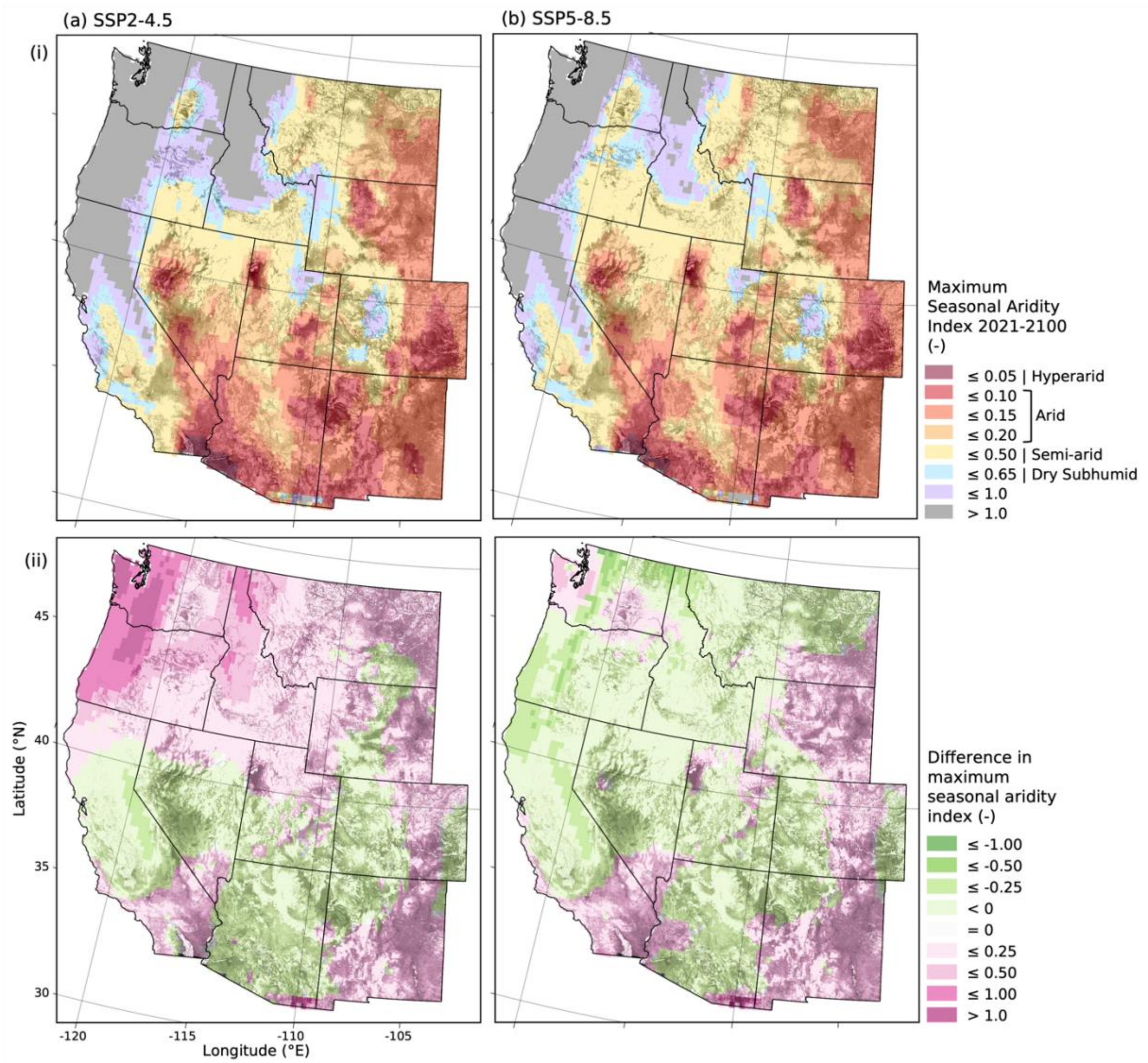

Figure 22: Maximum mean seasonal aridity index for the projected time period (2021-2100) (row i), and the difference in maximum mean seasonal aridity index from the historical period (1991-2010) to the maximum mean seasonal aridity index in the projected time period (row ii) for SSP2-4.5 (column a) and SSP5-8.5 (column b). For all plots, the color scheme is described by row and indicates the aridity index variables. The colors are semi-transparent and overly a grayscale of the minimum required cover thickness derived from 95th percentile required water storage ($L_{V3,95}$) ranging from required thickness near 0 m (darkest) to 5 m (lightest). Areas with a minimum required cover thickness greater than 5 m are not displayed.

Maximum seasonal aridity index is the maximum fraction of precipitation divided by PET on a seasonal time step. Maximum seasonal aridity index over the entire projected time period from 2021-2100, the most humid season within the projected period, indicates that regions in the coastal Pacific Northwest, Sierra Nevada Range, Cascade Range, and Northern Rocky Mountains have seasons where total precipitation exceeds PET (Figure 22). Regions in the Sonoran Desert have maximum seasonal aridity index values that are still considered hyperarid. Approximately 30% of the land area in the Western US is projected to have a maximum aridity index of 0.20 or less, indicating that this area is projected to remain arid to hyperarid. This classification broadly corresponds to where existing burial potential is indicated by minimum required cover thickness depths less than 5 m.

The difference between the maximum seasonal aridity index in the historical period and the projected period (historical maximum minus projected period maximum) indicates how the highest ratio of precipitation to PET may change over time. Under SSP2-4.5, much of the land area is projected to have up to 0.25 higher (more humid) maximum aridity index values (Figure 22a, i). Increases in maximum seasonal aridity index greater than 1 are projected in the Pacific Northwest and along the southern Arizona border. Maximum seasonal aridity index values in central California, central Nevada, southern Utah, Arizona, and parts of Montana, Wyoming, Colorado, and New Mexico are projected to moderately decrease (more arid) by up to -0.25. Maximum seasonal aridity index is projected to decrease up to -1 in the Sierra Nevada Range. Under SSP5-8.5, a majority of the land area of the Western US is projected to have a decrease in maximum seasonal aridity index of up to -0.25, with decreases greater in magnitude than 1 occurring in the Cascade Range, Coast Ranges, and Sierra Nevada Mountains. Maximum seasonal aridity index is projected to increase by up to 0.50 in parts of the Olympic Peninsula and Eastern Washington, the Sonoran Desert, the plains of southeastern Montana and eastern Wyoming, central Colorado, and most of New Mexico. The greatest increases in projected maximum seasonal aridity index for both SSPs occur in the high elevation regions in southern Arizona and New Mexico with projected increases over 1.

3.4 Discussion

On an annual scale, precipitation and applied water are projected to increase under both climate change scenarios by 20 to 50%. Seasonally, precipitation is projected to decrease in the spring months in the southern Western US, in the summer months in the northeastern region of the Western US under both climate change scenarios, and in the winter months in southern California, Arizona, and New Mexico. Projected precipitation increases are positively correlated with elevation, with mountain ranges expected to see the largest increases in precipitation. These regions also predominantly have higher precipitation in the historical period, and when looking at percent change, the intermountain West between the western slope of the Rocky Mountains and eastern slope of the Cascade and Sierra Nevada Ranges shows the greatest percent increase in precipitation.

When comparing predicted changes in precipitation and applied water, the influence of winter snowpack becomes evident. In the historical period, snowpack at high elevations evidently stores water from winter precipitation events until it is applied in the spring when the snowpack melts. In mountainous regions where historical snowpack is significant, winter applied water is projected to increase by ~200-300 mm while spring applied water is projected to decrease by a similar magnitude. Looking on a monthly time scale, increases in applied water are projected from November through March, but significant decreases are projected in April and May with magnitudes of change up to ~200 mm per month. In the historical period, snowmelt corresponded with the months of April and May. These results suggest that significantly less precipitation will fall as snow or that snow is not stored as snowpack for month-long timescales, which corroborates observational and other model-based studies (Trujillo and Molotch, 2014; Huning and AghaKouchak, 2018). These results have significant implications for regional water balance including water availability, streamflow, and wildfire implications. However, for woody biomass burial, these changes likely aren't critical because these areas are generally excluded from suitable locations for burial to begin with because the pulse of applied water from snowpack results in high required burial depths.

PET is projected to increase on the annual timestep and on all seasonal timesteps with the exception of parts of California, Nevada, and Arizona in the summer season under SSP5-8.5 where a slight decrease in PET is observed. The implications of this are largely positive for the potential of woody biomass burial since an increase in PET would increase the atmospheric demand of water from the soil column. In the areas of California, Nevada, and Arizona that show a slight decrease in PET in the summer under SSP5-8.5, the impact is likely negligible because these regions have high total summer seasonal PET (> 1000 mm) and very low total summer precipitation (0-200 mm) in the historical period.

The largest PET increases occur in the mountain ranges, and this is likely related to the reduction in snowpack. Snowpack is explicitly modeled in the applied water framework, and the presence or absence of snowpack informs the albedo coefficient for shortwave radiation in the net radiation module of the PET model. Shortwave radiation is the largest component of incoming energy to the modeled system, so a change in albedo of 0.49 from snowpack albedo of 0.74 to a bare surface albedo of 0.25 represents a large change in how much energy is reflected out of the modeled system. The loss of snowpack earlier in the year with an increase in PET may result in drier soil columns in the spring, and this may have implications for wildfire risk with earlier melt off and drier conditions.

Applied water is critical for accounting for the temporal distribution of water in regions where there is snowpack. On large geospatial scales, most of the regions affected by significant snow have low burial biomass burial potential, likely due to the pulse of applied water during spring melt, but snow should be accounted for in all regions that experience it. Deriving a monthly and seasonal index that looks at the timing and magnitude of applied water and PET would likely produce more accurate predictions of changes in conditions with climate change than the precipitation-based aridity index.

Mean annual aridity index is projected to increase (more humid) in by the end-century time period in the majority of the Western US under both SSPs, but this change is generally small (< 0.10). Broadly, the region west of the Rocky Mountains is projected to have an increase (more humid) in mean annual aridity index over each time period while the Great Plains region east of the Rocky Mountains is projected to have a decrease (more arid) in mean annual aridity index. However, the magnitudes of change are small, and when looking at the classification of aridity index using UNEP (1992) guidelines, only the hyperarid classification experiences a small decrease in area. The change in maximum seasonal aridity index from the historical period to the projected period has very different geospatial distributions under SSP2-4.5 and SSP5-8.5, as discussed in the results. Broadly, when interpreting the projected maximum seasonal aridity index with the historical minimum required cover thickness, it is evident that most of the regions with required cover thicknesses less than 5 m fall in regions that have both historically been and are projected to be within arid or hyperarid aridity classifications. This is supportive of the possibility for woody biomass burial in these areas through the end of the 21st century despite a slight annual trend towards more humid conditions.

The timing of precipitation and applied water relative to PET are critical to understand regional water balance. For example, the Great Plains east of the Rocky Mountains show high woody biomass burial potential with low required cover thickness despite having higher mean annual precipitation than many of the regions in the desert Southwest. This is because precipitation in the Great Plains is highly seasonal with a significant summer peak that corresponds to the peak in PET (Lauenroth and Bradford, 2006). Warm temperature, small precipitation events, and plant transpiration prevent water from reaching deeper storage in the soil column. Summer precipitation in the Great Plains is driven by the weakening of the prevailing Westerly winds allowing the warm, wet air to move up from the Gulf of Mexico as part of the circulation around the permanent subtropical high-pressure system in the Atlantic Ocean. The future climate modeling indicates that this driving mechanism will likely remain into the 21st century, supporting potential for burial in the Great Plains in the future, especially given the projected decrease in aridity index. However, given that there isn't significant woody biomass in the Great Plains, the transportation distance from forests thinned for high wildfire risk to sites suitable for burial may be significant, and this would need to be accounted for in the life cycle analysis to show carbon storage. This example also illustrates how factors beyond the climatological ones described here need to be critically analyzed and taken into account if woody biomass burial is going to result in net carbon storage.

Within the climatological modeling presented here, there are key assumptions that affect the interpretation of the resulting model outputs. First, the interpretation of the aridity index is limited by the choice of equation and parameterization of PET (Federer et al., 1996; Kingston et al., 2009; Song et al., 2022). Previous research, including trials run during this research but not described in text, has demonstrated that various PET equations and parameterizations can change the resulting PET estimates by several hundred millimeters on annual time scales (Federer et al., 1996). While care was taken to select and parameterize the Penman PET methodology presented here, it is critical to note the dependence of aridity index on PET and the dependence of PET on the methodology of calculation. An early study with CMIP3 data found that while all six PET methods tested indicated an increase in PET, the selection of equation and parameterization of PET was a determinant in the direction of aridity index changes in future time periods (Kingston et al., 2009). Modeling work in the Great Plains found that more physically based approaches for calculating PET tended to show weaker drying trends (Yuan and Quiring, 2014). PET is sensitive to changes in temperature, but this sensitivity also varies by PET equation, with the Penman approach being considered as moderately sensitive to temperature (Sutapa et al., 2020). It therefore appears likely that the question is not whether PET will increase, but how the pace of this increase relates to the increase in precipitation predicted in climate models. This has critical implications for woody biomass burial given that there is a possible range of PET outcomes from the same projected climatological inputs depending on methods of calculation. A sensitivity analysis on the methodology and parameterization presented here should be considered before using the aridity index to make decisions about potential for woody biomass burial under future climates.

Numerous assumptions are necessary to build a geospatial implementation of PET across a large, diverse landscape. In this model, we use a vegetation height of 1 m to generate a roughness height of 0.1 m. This 1 m assumption is based on the approximate height of shrubby vegetation found in the regions that appeared plausible for woody biomass burial in Section 2. Roughness height informs the scaling of wind speed from a 10 m height as it is modeled within GCMs to a 2 m height as is used in PET equations using natural log transforms. If the modelled vegetation height is shorter than the actual vegetation height, surface wind speed will be overestimated, leading to higher PET values. The reverse is true if the modelled vegetation height is taller than the actual vegetation height: surface wind speed will be underestimated resulting in lower PET values.

Since albedo controls how much of the incoming energy stays within the system, it can have large impacts on the results of PET, as touched on briefly in the context of snowpack earlier. When regions were not covered in snowpack, we assumed a global albedo of 0.25 which was found to be representative of semi-desert ecosystems (Douglas et al., 2009). By land area, semi-desert or arid regions make up the majority of the Western US, but the use of global albedo decoupled from vegetation type at each pixel likely results in over and under estimation of PET in regions with different land cover types. Bare ground in deserts has a higher albedo, estimated around 0.30, so PET in deserts is likely underestimated in this model (McVicar et al., 2007). In contrast, coniferous forests can have albedo values near 0.10, so PET in these regions is likely overestimated by this model (Douglas et al., 2009). If future climate predictions for woody biomass burial are being seriously analyzed in regions outside of arid or semi-arid environments, a sensitivity analysis should be performed on the effect of albedo in the PET model, and the user should consider using albedo values specific to the land cover type of interest or varying the albedo spatially. Additionally, land cover type will likely change with climate change, and this change over time would need to be accounted for if spatially explicit albedo is used within the PET model.

Beyond the formulation and parameterization of the PET model, there are limitations and uncertainties within the climate models themselves that inform the input data for the PET model. GCMs produce more frequent precipitation events than observed (Stephens et al., 2010). Warmer air temperatures are expected to result in more water being held in the atmosphere following the Clausius-Clapeyron relationship between temperature and saturation vapor pressure, and this relationship is quantified in GCMs. However, the observed humidity trends within arid and semiarid regions, both globally and in the Western US, are significantly lower in magnitude than the Clausius-Clapeyron relationship would suggest and thus don't match the climate model projections over the time period where climate modeling and observational data overlap (Simpson et al., 2023). This suggests that in arid and semiarid areas, there isn't enough water to meet the atmospheric demand, but this isn't captured in climate modeling. Recent research suggests that conditions in arid regions will likely be even more arid in future time periods (Allan and Douville, 2023). This work calls into question the direction and magnitude of the projected change in aridity index throughout the 21st century presented here. The results presented here likely represent the more humid limit of possible outcomes, and as such, they likely conservatively model locations suited for woody biomass burial in the future. While more arid conditions in the future support the possibility for successful woody biomass burial, it is critical to understand that climate models do not currently capture key components of the hydrological forcing of arid and semiarid regions. This reinforces the need for any biomass burial to have active management and careful monitoring of climatic and burial conditions into the future.

3.5 Conclusion

We modeled PET using CMIP6 meteorological projections for a 26 multi-model ensemble, returning reasonable calculations using the Penman (1948) model parameterized for semi-arid environments in the Western US. Given the limitations of climate modeling and the complexity of parameterizing a heterogeneous landscape such as the Western US, we did not utilize existing published methods to approximate AET from PET. Instead, aridity index, the ratio between accumulated precipitation and PET, was used to understand the relative magnitudes of water applied to regions and the corresponding atmospheric demand.

The applied water, water balance, and PET models developed herein produce reasonable estimates of the quantities they seek to capture. Changes in applied water indicate that snowpack will likely either diminish entirely or spring snowmelt will move forward by the end-century time period under both SSPs. Both precipitation and PET are projected to increase on an annual time step from the historical baseline, and when looking at aridity index, a majority of the Western US is projected to become slightly more humid on an annual timestep. These trends are stronger under SSP5-8.5 than SSP2-4.5. The aridity index trend is small and previous studies have identified ways in which PET results from climate modeling can produce aridity index trends in opposing directions depending on the PET methodology used. As such, we have low confidence in the overall indication of a slightly wetter condition in the Western US under climate change scenarios. Even still, under the most humid seasonal conditions, there are still regions that are projected to become more arid which is indicative of the climatological potential for woody biomass burial.

4. Overall Conclusions and Future Work

From the geospatial modeling presented here, there appears to be an opportunity for woody biomass burial from a macroclimate perspective, based on both historical and future climate scenarios. While this work provides a broad overview of burial potential, more detailed climate modeling and site-specific modeling will be critical. The analysis presented here does not quantify drought or precipitation extremes, and these topics are critical next steps to understand future moisture conditions in the Western US. The datasets derived here can be used to describe far more about the possible future conditions of the Western US, far beyond what is described in this thesis. Beyond the climatological perspective focused on in this thesis, many other considerations need to be accounted for before implementing woody biomass burial. These considerations range from other geophysical factors like microclimate, precipitation runoff, wind transfer of moisture, subsurface groundwater, and depth of bedrock to ecological considerations of ecosystem disturbance to social, economic, and practical considerations such as land ownership, environmental justice, and existing infrastructure. Detailed life cycle analyses should be created before implementation to account for greenhouse gas emissions from soil disturbance, biomass transportation, and machinery among other factors. If biomass burial is implemented, monitoring, reporting, and verification (MRV) over time will be critical to ensure that decay and carbon emissions are carefully monitored and minimized. Woody biomass burial in the Western US represents an opportunity to durably store carbon from wood thinned from high wildfire risk forests. This thesis indicates that there are regions across the Western US that are climatologically suited to woody biomass burial due to their aridity both now and under projected climates through 2100.

5. Acknowledgements

A massive thank you to my advisor, Sinéad Crotty, for her expertise, support, and enthusiasm for my research and for broadly pushing forward the scientific frontier in biomass carbon removal and storage. Thank you to Alex Wyckoff for being a great collaborator and mentor and for his massive contribution to this project beyond the climatological aspects presented here. Thank you to Alexey Fedorov and Jacob Stuivenvolt-Allen for help getting started with high performance computing and CMIP6 modeling. Thank you to Matthew Eisaman for his time as my second reader. Thank you to Jenn Kasbohm, Pincelli Hull, and Maureen Long for their support of the undergraduate students in the EPS department – it doesn't go unnoticed! Finally, thank you to all my incredible friends and family who have supported me throughout my time at Yale.

6. References

Abatzoglou, J. T., & Williams, A. P. (2016). Impact of anthropogenic climate change on wildfire across western US forests. *Proceedings of the National Academy of Sciences*, *113*(42), 11770–11775. https://doi.org/10.1073/pnas.1607171113

Adair, E. C., Parton, W. J., Del Grosso, S. J., Silver, W. L., Harmon, M. E., Hall, S. A., Burke, I. C., & Hart, S. C. (2008). Simple three-pool model accurately describes patterns of long-term litter decomposition in diverse climates. *Global Change Biology*, *14*(11), 2636–2660. https://doi.org/10.1111/j.1365-2486.2008.01674.x

Adams, D. K., & Comrie, A. C. (1997). The North American Monsoon. *Bulletin of the American Meteorological Society*, *78*(10), 2197–2214. https://doi.org/10.1175/1520-0477(1997)078<2197:TNAM>2.0.CO;2

Ajjur, S. B., & Al-Ghamdi, S. G. (2021). Evapotranspiration and water availability response to climate change in the Middle East and North Africa. *Climatic Change*, *166*(3), 28. https://doi.org/10.1007/s10584-021-03122-z

Albright, W. H., Benson, C. H., & Waugh, W. J. (2010). *Water balance covers for waste containment: Principles and practice*. American Society of Civil Engineers (ASCE).

Allan, R. P., & Douville, H. (2024). An even drier future for the arid lands. *Proceedings of the National Academy of Sciences*, *121*(2), e2320840121. https://doi.org/10.1073/pnas.2320840121

Allen, R. G., Pereira, L. S., Raes, D., & Smith, M. (1998). *Crop evapotranspiration: Guidelines for computing crop water requirements* (56; FAO Irrigation and Drainage). Food and Agriculture Organization of the United Nations. https://www.fao.org/3/X0490E/x0490e00.htm

Apiwantragoon, P. (2007). *Field hydrologic evaluation of final covers for waste containment*. University of Wisconsin - Madison.

Bendz, D. (1998). *Generation of leachate and the flow regime in landfills* (1023; p. 151). Department of Water Resources Engineering, Lund Institute of Technology, Lund University. https://www.osti.gov/etdeweb/servlets/purl/646189

Berg, A., & Sheffield, J. (2019). Evapotranspiration Partitioning in CMIP5 Models: Uncertainties and Future Projections. *Journal of Climate*, *32*(10), 2653–2671. https://doi.org/10.1175/JCLI-D-18-0583.1

Broberg, L. (2021). Relative snowpack response to elevation, temperature and precipitation in the Crown of the Continent region of North America 1980-2013. *PLOS ONE*, *16*(4), e0248736. https://doi.org/10.1371/journal.pone.0248736

Cable, J. M., Ogle, K., Williams, D. G., Weltzin, J. F., & Huxman, T. E. (2008). Soil Texture Drives Responses of Soil Respiration to Precipitation Pulses in the Sonoran Desert: Implications for Climate Change. *Ecosystems*, *11*(6), 961–979. https://doi.org/10.1007/s10021-008-9172-x

Chegini, T., Li, H.-Y., & Leung, L. R. (2021). HyRiver: Hydroclimate Data Retriever. *Journal of Open Source Software*, *6*(66), 3175. https://doi.org/10.21105/joss.03175

Choudhury, BhaskarJ. (1999). Evaluation of an empirical equation for annual evaporation using field observations and results from a biophysical model. *Journal of Hydrology*, *216*(1), 99–110. https://doi.org/10.1016/S0022-1694(98)00293-5

Cleugh, H. A., Leuning, R., Mu, Q., & Running, S. W. (2007). Regional evaporation estimates from flux tower and MODIS satellite data. *Remote Sensing of Environment*, *106*(3), 285–304. https://doi.org/10.1016/j.rse.2006.07.007

Colle, B. A., Smith, R. B., & Wesley, D. A. (2013). Theory, Observations, and Predictions of Orographic Precipitation. In F. K. Chow, S. F. J. De Wekker, & B. J. Snyder (Eds.), *Mountain Weather Research and Forecasting: Recent Progress and Current Challenges* (pp. 291–344). Springer Netherlands. https://doi.org/10.1007/978-94-007-4098-3_6

Curley, P. G., Adams, E. E., & McKittrick, L. R. (2014). The Influence of Solar Radiation Attenuation in Snow on Near Surface Energy Balance in Complex Topography. *International Snow Science Workshop 2014 Proceedings, Banff, Canada*, 567–573.

Cusack, D. F., Chou, W. W., Yang, W. H., Harmon, M. E., Silver, W. L., & Team, T. L. (2009). Controls on long-term root and leaf litter decomposition in neotropical forests. *Global Change Biology*, *15*(5), 1339–1355. https://doi.org/10.1111/j.1365-2486.2008.01781.x

Davies, J. H., & Davies, D. R. (2010). Earth's surface heat flux. *Solid Earth*, *1*(1), 5–24. https://doi.org/10.5194/se-1-5-2010

Dettinger, M. (2011). Climate Change, Atmospheric Rivers, and Floods in California – A Multimodel Analysis of Storm Frequency and Magnitude Changes1. *JAWRA Journal of the American Water Resources Association*, *47*(3), 514–523. https://doi.org/10.1111/j.1752-1688.2011.00546.x

Dingman, S. L. (1992). *Physical Hydrology*. Prentice Hall.

Douglas, E. M., Jacobs, J. M., Sumner, D. M., & Ray, R. L. (2009). A comparison of models for estimating potential evapotranspiration for Florida land cover types. *Journal of Hydrology*, *373*(3), 366–376. https://doi.org/10.1016/j.jhydrol.2009.04.029

Evans, S. L., Flores, A. N., Heilig, A., Kohn, M. J., Marshall, H.-P., & McNamara, J. P. (2016). Isotopic evidence for lateral flow and diffusive transport, but not sublimation, in a sloped seasonal snowpack, Idaho, USA. *Geophysical Research Letters*, *43*(7), 3298–3306. https://doi.org/10.1002/2015GL067605

Fayer, M. J. (2000). *UNSAT-H Version 3.0:Unsaturated Soil Water and Heat Flow Model Theory, User Manual, and Examples* (820201000). Pacific Northwest National Lab. (PNNL), Richland, WA (United States). https://doi.org/10.2172/781853

Federer, C. A., Vörösmarty, C., & Fekete, B. (1996). Intercomparison of Methods for Calculating Potential Evaporation in Regional and Global Water Balance Models. *Water Resources Research*, *32*(7), 2315–2321. https://doi.org/10.1029/96WR00801

Fingerman, K. R., Qiriazi, J., Barrientos, C. L., Blasdel, M., Comnick, J. M., Harris, A. R., Geronimo, C., Hsu, C.-W., Kane, J. M., Oneil, E., Rios-Romero, S., Rogers, L. W., Severy, M., & Wright, M. C. (2023). Climate and air pollution impacts of generating biopower from forest management residues in California. *Environmental Research Letters*, *18*(3), 034038. https://doi.org/10.1088/1748-9326/acbd93

Gholz, H. L., Wedin, D. A., Smitherman, S. M., Harmon, M. E., & Parton, W. J. (2000). Long-term dynamics of pine and hardwood litter in contrasting environments: Toward a global model of decomposition. *Global Change Biology*, *6*(7), 751–765. https://doi.org/10.1046/j.1365-2486.2000.00349.x

Gooding, J. L. (2023). Geologic perspective for carbon sequestration by woody biomass burial. *Science and Technology for Energy Transition*, *78*, 17. https://doi.org/10.2516/stet/2023014

Higgins, R. W., Yao, Y., & Wang, X. L. (1997). Influence of the North American Monsoon System on the U.S. Summer Precipitation Regime. *Journal of Climate*, *10*(10), 2600–2622. https://doi.org/10.1175/1520-0442(1997)010<2600:IOTNAM>2.0.CO;2

Homer, C. G., Fry, J. A., & Barnes, C. A. (2012). The National Land Cover Database. In *Fact Sheet* (2012–3020). U.S. Geological Survey. https://doi.org/10.3133/fs20123020

Hoyer, S., & Hamman, J. (2017). xarray: N-D labeled Arrays and Datasets in Python. *Journal of Open Research Software*, *5*(1). https://doi.org/10.5334/jors.148

Huang, X., Swain, D. L., & Hall, A. D. (2020). Future precipitation increase from very high resolution ensemble downscaling of extreme atmospheric river storms in California. *Science Advances*, *6*(29), eaba1323. https://doi.org/10.1126/sciadv.aba1323

Huning, L. S., & AghaKouchak, A. (2018). Mountain snowpack response to different levels of warming. *Proceedings of the National Academy of Sciences*, *115*(43), 10932–10937. https://doi.org/10.1073/pnas.1805953115

IPCC. (2023). *Climate Change 2023: Synthesis Report: Contribution of Working Groups I, II and III to the Sixth Assessment Report of the Intergovernmental Panel on Climate Change* (pp. 35–115). IPCC. https://dx.doi.org/10.59327/IPCC/AR6-9789291691647

Jackson, S. T., & Overpeck, J. T. (2000). Responses of Plant Populations and Communities to Environmental Changes of the Late Quaternary. *Paleobiology*, *26*(4), 194–220.

Joly, F.-X., Scherer-Lorenzen, M., & Hättenschwiler, S. (2023). Resolving the intricate role of climate in litter decomposition. *Nature Ecology & Evolution*, *7*(2), Article 2. https://doi.org/10.1038/s41559-022-01948-z

Kampf, S. K., McGrath, D., Sears, M. G., Fassnacht, S. R., Kiewiet, L., & Hammond, J. C. (2022). Increasing wildfire impacts on snowpack in the western U.S. *Proceedings of the National Academy of Sciences*, *119*(39), e2200333119. https://doi.org/10.1073/pnas.2200333119

Khire, M. V., Benson, C. H., & Bosscher, P. J. (1997). Water Balance Modeling of Earthen Final Covers. *Journal of Geotechnical and Geoenvironmental Engineering*, *123*(8), 744–754. https://doi.org/10.1061/(ASCE)1090-0241(1997)123:8(744)

Kim, J., Waliser, D. E., Neiman, P. J., Guan, B., Ryoo, J.-M., & Wick, G. A. (2013). Effects of atmospheric river landfalls on the cold season precipitation in California. *Climate Dynamics*, *40*(1), 465–474. https://doi.org/10.1007/s00382-012-1322-3

Kingston, D. G., Todd, M. C., Taylor, R. G., Thompson, J. R., & Arnell, N. W. (2009). Uncertainty in the estimation of potential evapotranspiration under climate change. *Geophysical Research Letters*, *36*(20). https://doi.org/10.1029/2009GL040267

Kopp, G., & Lean, J. L. (2011). A new, lower value of total solar irradiance: Evidence and climate significance. *Geophysical Research Letters*, *38*(1). https://doi.org/10.1029/2010GL045777

Kustas, W. P., Rango, A., & Uijlenhoet, R. (1994). A simple energy budget algorithm for the snowmelt runoff model. *Water Resources Research*, *30*(5), 1515–1527. https://doi.org/10.1029/94WR00152

Lauenroth, W. K., & Bradford, J. B. (2006). Ecohydrology and the Partitioning AET Between Transpiration and Evaporation in a Semiarid Steppe. *Ecosystems*, *9*(5), 756–767. https://doi.org/10.1007/s10021-006-0063-8

Lauenroth, W. K., & Bradford, J. B. (2009). Ecohydrology of dry regions of the United States: Precipitation pulses and intraseasonal drought. *Ecohydrology*, *2*(2), 173–181. https://doi.org/10.1002/eco.53

Lauenroth, W. K., Schlaepfer, D. R., & Bradford, J. B. (2014). Ecohydrology of Dry Regions: Storage versus Pulse Soil Water Dynamics. *Ecosystems*, *17*(8), 1469–1479. https://doi.org/10.1007/s10021-014-9808-y

Leung, L. R., & Qian, Y. (2009). Atmospheric rivers induced heavy precipitation and flooding in the western U.S. simulated by the WRF regional climate model. *Geophysical Research Letters*, *36*(3). https://doi.org/10.1029/2008GL036445

Li, D., Pan, M., Cong, Z., Zhang, L., & Wood, E. (2013). Vegetation control on water and energy balance within the Budyko framework. *Water Resources Research*, *49*(2), 969–976. https://doi.org/10.1002/wrcr.20107

Li, S., Kang, S., Zhang, L., Zhang, J., Du, T., Tong, L., & Ding, R. (2016). Evaluation of six potential evapotranspiration models for estimating crop potential and actual evapotranspiration in arid regions. *Journal of Hydrology*, *543*, 450–461. https://doi.org/10.1016/j.jhydrol.2016.10.022

Linacre, E. T. (1993). Data-sparse estimation of lake evaporation, using a simplified Penman equation. *Agricultural and Forest Meteorology*, *64*(3), 237–256. https://doi.org/10.1016/0168-1923(93)90031-C

Lu, J., Sun, G., McNulty, S. G., & Amatya, D. M. (2005). A Comparison of Six Potential Evapotranspiration Methods for Regional Use in the Southeastern United States1. *JAWRA Journal of the American Water Resources Association*, *41*(3), 621–633. https://doi.org/10.1111/j.1752-1688.2005.tb03759.x

Martin, J. T., Pederson, G. T., Woodhouse, C. A., Cook, E. R., McCabe, G. J., Anchukaitis, K. J., Wise, E. K., Erger, P. J., Dolan, L., McGuire, M., Gangopadhyay, S., Chase, K. J., Littell, J. S., Gray, S. T., St. George, S., Friedman, J. M., Sauchyn, D. J., St-Jacques, J.-

M., & King, J. (2020). Increased drought severity tracks warming in the United States' largest river basin. *Proceedings of the National Academy of Sciences*, *117*(21), 11328–11336. https://doi.org/10.1073/pnas.1916208117

Martinec, J. (1989). Hour-to-hour snowmelt rates and lysimeter outflow during an entire ablation period, in Snow Cover and Glacier Variations. In A. Rango (Ed.), *Proceedings of the Baltimore Symposium* (Vol. 183, pp. 19–28). IAHS Publ.

Martínez-Cob, A., & Tejero-Juste, M. (2004). A wind-based qualitative calibration of the Hargreaves ET0 estimation equation in semiarid regions. *Agricultural Water Management*, *64*(3), 251–264. https://doi.org/10.1016/S0378-3774(03)00199-9

McMahon, T. A., Peel, M. C., Lowe, L., Srikanthan, R., & McVicar, T. R. (2013). Estimating actual, potential, reference crop and pan evaporation using standard meteorological data: A pragmatic synthesis. *Hydrology and Earth System Sciences*, *17*(4), 1331–1363. https://doi.org/10.5194/hess-17-1331-2013

McVicar, T. R., Van Niel, T. G., Li, L., Hutchinson, M. F., Mu, X., & Liu, Z. (2007). Spatially distributing monthly reference evapotranspiration and pan evaporation considering topographic influences. *Journal of Hydrology*, *338*(3), 196–220. https://doi.org/10.1016/j.jhydrol.2007.02.018

Meentemeyer, V. (1978). Macroclimate and Lignin Control of Litter Decomposition Rates. *Ecology*, *59*(3), 465–472. https://doi.org/10.2307/1936576

Milly, P. C. D. (1994). Climate, soil water storage, and the average annual water balance. *Water Resources Research*, *30*(7), 2143–2156. https://doi.org/10.1029/94WR00586

Milly, P. C. D., & Dunne, K. A. (2020). Colorado River flow dwindles as warming-driven loss of reflective snow energizes evaporation. *Science*, *367*(6483), 1252–1255. https://doi.org/10.1126/science.aay9187

Neiman, P. J., Schick, L. J., Ralph, F. M., Hughes, M., & Wick, G. A. (2011). Flooding in Western Washington: The Connection to Atmospheric Rivers. *Journal of Hydrometeorology*, *12*(6), 1337–1358. https://doi.org/10.1175/2011JHM1358.1

Overpeck, J. T., & Udall, B. (2020). Climate change and the aridification of North America. *Proceedings of the National Academy of Sciences*, *117*(22), 11856–11858. https://doi.org/10.1073/pnas.2006323117

Parton, W., Silver, W. L., Burke, I. C., Grassens, L., Harmon, M. E., Currie, W. S., King, J. Y., Adair, E. C., Brandt, L. A., Hart, S. C., & Fasth, B. (2007). Global-Scale Similarities in Nitrogen Release Patterns During Long-Term Decomposition. *Science*, *315*(5810), 361–364. https://doi.org/10.1126/science.1134853

Peng, L., Zeng, Z., Wei, Z., Chen, A., Wood, E. F., & Sheffield, J. (2019). Determinants of the ratio of actual to potential evapotranspiration. *Global Change Biology*, *25*(4), 1326–1343. https://doi.org/10.1111/gcb.14577

Penman, H. L. (1956). Evaporation: An introductory survey. *Netherlands Journal of Agricultural Science*, *4*(1), Article 1. https://doi.org/10.18174/njas.v4i1.17768

Penman, H. L., & Keen, B. A. (1997). Natural evaporation from open water, bare soil and grass. *Proceedings of the Royal Society of London. Series A. Mathematical and Physical Sciences*, *193*(1032), 120–145. https://doi.org/10.1098/rspa.1948.0037

Phillips, M. (2013). *Estimates of sublimation in the Upper Colorado River basin* [M.S., Colorado State University]. https://www.proquest.com/docview/1496773077/abstract/CECB9DDFE2E24B9CPQ/1

Riahi, K., van Vuuren, D. P., Kriegler, E., Edmonds, J., O'Neill, B. C., Fujimori, S., Bauer, N., Calvin, K., Dellink, R., Fricko, O., Lutz, W., Popp, A., Cuaresma, J. C., Kc, S., Leimbach, M., Jiang, L., Kram, T., Rao, S., Emmerling, J., … Tavoni, M. (2017). The Shared Socioeconomic Pathways and their energy, land use, and greenhouse gas emissions implications: An overview. *Global Environmental Change*, *42*, 153–168. https://doi.org/10.1016/j.gloenvcha.2016.05.009

Running, S. W., & Coughlan, J. C. (1988). A general model of forest ecosystem processes for regional applications I. Hydrologic balance, canopy gas exchange and primary production processes. *Ecological Modelling*, *42*(2), 125–154. https://doi.org/10.1016/0304-3800(88)90112-3

Sandalow, D., Aines, R., Friedmann, J., McCormick, C., & Sanchez, D. (2021). *Biomass Carbon Removal and Storage (BiRCS) Roadmap* (LLNL-TR--815200, 1763937, 1024342; p. 65). Lawrence Livermore National Laboratory. https://doi.org/10.2172/1763937

Schmidt, R. A., & Gluns, D. R. (1992). *Sublimation of Snow—The Basics* (p. 7). University of Montana. https://arc.lib.montana.edu/snow-science/objects/issw-1992-011-017.pdf

Senay, G. B., Bohms, S., Singh, R. K., Gowda, P. H., Velpuri, N. M., Alemu, H., & Verdin, J. P. (2013). Operational Evapotranspiration Mapping Using Remote Sensing and Weather Datasets: A New Parameterization for the SSEB Approach. *JAWRA Journal of the American Water Resources Association*, *49*(3), 577–591. https://doi.org/10.1111/jawr.12057

Senay, G. B., Friedrichs, M., Morton, C., Parrish, G. E. L., Schauer, M., Khand, K., Kagone, S., Boiko, O., & Huntington, J. (2022). Mapping actual evapotranspiration using Landsat for the conterminous United States: Google Earth Engine implementation and assessment of the SSEBop model. *Remote Sensing of Environment*, *275*, 113011. https://doi.org/10.1016/j.rse.2022.113011

Senay, G. B., & Kagone, S. (2019). *Daily SSEBop Evapotranspiration: U. S. Geological Survey Data Release* [dataset]. U.S. Geological Survey. https://doi.org/10.5066/P9L2YMV

Sheffield, J., Goteti, G., & Wood, E. F. (2006). Development of a 50-Year High-Resolution Global Dataset of Meteorological Forcings for Land Surface Modeling. *Journal of Climate*, *19*(13), 3088–3111. https://doi.org/10.1175/JCLI3790.1

Simões, C. L., Simoes, R., Gonçalves, A. S., & Nunes, L. J. R. (2023). Environmental Analysis of the Valorization of Woody Biomass Residues: A Comparative Study with Vine Pruning Leftovers in Portugal. *Sustainability*, *15*(20), Article 20. https://doi.org/10.3390/su152014950

Simpson, I. R., McKinnon, K. A., Kennedy, D., Lawrence, D. M., Lehner, F., & Seager, R. (2024). Observed humidity trends in dry regions contradict climate models. *Proceedings of the National Academy of Sciences*, *121*(1), e2302480120. https://doi.org/10.1073/pnas.2302480120

Simunek, J. M., M. Th Van Genuchten, & M. Sejna. (2005). The HYDRUS-1D software package for simulating the one-dimensional movement of water, heat, and multiple solutes in variably-saturated media. *University of California-Riverside Research Reports*, *3*, 240.

Smith, P. (2016). Soil carbon sequestration and biochar as negative emission technologies. *Global Change Biology*, *22*(3), 1315–1324. https://doi.org/10.1111/gcb.13178

Smith, R. B. (2006). Progress on the theory of orographic precipitation. In S. D. Willett, N. Hovius, M. T. Brandon, & D. M. Fisher (Eds.), *Tectonics, Climate, and Landscape Evolution* (Vol. 398, p. 0). Geological Society of America. https://doi.org/10.1130/2006.2398(01)

Soil Survey Staff. (2023). *Gridded National Soil Survey Geographic (gNATSGO) Database for the Conterminous United States* (Version FY2024) [dataset]. U.S. Department of Agriculture, Natural Resources Conservation Service. https://nrcs.app.box.com/v/soils

Song, Y. H., Chung, E.-S., & Shahid, S. (2022). Uncertainties in evapotranspiration projections associated with estimation methods and CMIP6 GCMs for South Korea. *Science of The Total Environment*, *825*, 153953. https://doi.org/10.1016/j.scitotenv.2022.153953

Stephens, G. L., L'Ecuyer, T., Forbes, R., Gettelmen, A., Golaz, J.-C., Bodas-Salcedo, A., Suzuki, K., Gabriel, P., & Haynes, J. (2010). Dreary state of precipitation in global models. *Journal of Geophysical Research: Atmospheres*, *115*(D24). https://doi.org/10.1029/2010JD014532

Stevenson, A., Cray, J. A., Williams, J. P., Santos, R., Sahay, R., Neuenkirchen, N., McClure, C. D., Grant, I. R., Houghton, J. D., Quinn, J. P., Timson, D. J., Patil, S. V., Singhal, R. S., Antón, J., Dijksterhuis, J., Hocking, A. D., Lievens, B., Rangel, D. E. N., Voytek, M. A., … Hallsworth, J. E. (2015). Is there a common water-activity limit for the three domains of life? *The ISME Journal*, *9*(6), 1333–1351. https://doi.org/10.1038/ismej.2014.219

Stewart, I. T. (2009). Changes in snowpack and snowmelt runoff for key mountain regions. *Hydrological Processes*, *23*(1), 78–94. https://doi.org/10.1002/hyp.7128

Sutapa, I. W., Saparuddin, & Wicana, S. (2020). Sensitivity of methods for estimating potential evapotranspiration to climate change. *IOP Conference Series: Earth and Environmental Science*, *437*(1), 012039. https://doi.org/10.1088/1755-1315/437/1/012039

Svoma, B. M. (2015). Difficulties in Determining Snowpack Sublimation in Complex Terrain at the Macroscale. *Advances in Meteorology*, *2016*, e9695757. https://doi.org/10.1155/2016/9695757

Taheri, M., Mohammadian, A., Ganji, F., Bigdeli, M., & Nasseri, M. (2022). Energy-Based Approaches in Estimating Actual Evapotranspiration Focusing on Land Surface Temperature: A Review of Methods, Concepts, and Challenges. *Energies*, *15*(4), Article 4. https://doi.org/10.3390/en15041264

Thornton, M. M., Shrestha, R., Wei, Y., Thornton, P. E., & Kao, S.-C. (2022). Daymet: Daily Surface Weather Data on a 1-km Grid for North America, Version 4 R1. *ORNL DAAC*. https://doi.org/10.3334/ORNLDAAC/2129

Thornton, P. E., Hasenauer, H., & White, M. A. (2000). Simultaneous estimation of daily solar radiation and humidity from observed temperature and precipitation: An application over complex terrain in Austria. *Agricultural and Forest Meteorology*, *104*(4), 255–271. https://doi.org/10.1016/S0168-1923(00)00170-2

Thornton, P. E., Shrestha, R., Thornton, M., Kao, S.-C., Wei, Y., & Wilson, B. E. (2021). Gridded daily weather data for North America with comprehensive uncertainty quantification. *Scientific Data*, *8*(1), 190. https://doi.org/10.1038/s41597-021-00973-0

Thrasher, B., Maurer, E. P., McKellar, C., & Duffy, P. B. (2012). Technical Note: Bias correcting climate model simulated daily temperature extremes with quantile mapping.

Hydrology and Earth System Sciences, *16*(9), 3309–3314. https://doi.org/10.5194/hess-16-3309-2012

Thrasher, B., Wang, W., Michaelis, A., Melton, F., Lee, T., & Nemani, R. (2022). NASA Global Daily Downscaled Projections, CMIP6. *Scientific Data*, *9*(1), 262. https://doi.org/10.1038/s41597-022-01393-4

Trujillo, E., & Molotch, N. P. (2014). Snowpack regimes of the Western United States. *Water Resources Research*, *50*(7), 5611–5623. https://doi.org/10.1002/2013WR014753

United Nations Environment Programme. (1992). *World Atlas of Desertification*. Edward Arnold. https://wedocs.unep.org/xmlui/handle/20.500.11822/42137

U.S. Forest Service. (2022). *Confronting the Wildfire Crisis* (FS-1187a; p. 25). U.S. Department of Agriculture, Forest Service. https://www.fs.usda.gov/sites/default/files/fs_media/fs_document/Confronting-the-Wildfire-Crisis.pdf

U.S. Geological Survey. (2019). *3D Elevation Program 1-Meter Resolution Digital Elevation Model* [dataset]. https://www.usgs.gov/the-national-map-data-delivery

Woodall, C. M., & McCormick, C. F. (2022). Assessing the optimal uses of biomass: Carbon and energy price conditions for the Aines Principle to apply. *Frontiers in Climate*, *4*. https://doi.org/10.3389/fclim.2022.993230

Xu, C.-Y., & Singh, V. P. (2002). Cross Comparison of Empirical Equations for Calculating Potential Evapotranspiration with Data from Switzerland. *Water Resources Management*, *16*(3), 197–219. https://doi.org/10.1023/A:1020282515975

Yuan, S., & Quiring, S. M. (2014). Drought in the U.S. Great Plains (1980–2012): A sensitivity study using different methods for estimating potential evapotranspiration in the Palmer

Drought Severity Index. *Journal of Geophysical Research: Atmospheres*, *119*(19), 10,996-11,010. https://doi.org/10.1002/2014JD021970

Zeng, N. (2008). Carbon sequestration via wood burial. *Carbon Balance and Management*, *3*(1), 1. https://doi.org/10.1186/1750-0680-3-1

Zeng, N., & Hausmann, H. (2022). Wood Vault: Remove atmospheric CO2 with trees, store wood for carbon sequestration for now and as biomass, bioenergy and carbon reserve for the future. *Carbon Balance and Management*, *17*(1), 2. https://doi.org/10.1186/s13021-022-00202-0

Zeng, N., King, A. W., Zaitchik, B., Wullschleger, S. D., Gregg, J., Wang, S., & Kirk-Davidoff, D. (2013). Carbon sequestration via wood harvest and storage: An assessment of its harvest potential. *Climatic Change*, *118*(2), 245–257. https://doi.org/10.1007/s10584-012-0624-0